Mineralogy of autoclaved aerated concrete and characterization of tobermorite - advanced analytical methods and effect of changes in the chemical composition

Mineralogische Charakterisierung von Porenbeton und Tobermorit - verbesserte Analysemethoden und Einfluss veränderter chemischer Zusammensetzung

Der Naturwissenschaftlichen Fakultät der
Friedrich-Alexander-Universität Erlangen-Nürnberg
zur Erlangung des Doktorgrades
Dr. rer. nat

vorgelegt von

Jürgen Schreiner

aus Regensburg

Als Dissertation genehmigt von der Naturwissenschaftlichen
Fakultät der Friedrich-Alexander-Universität Erlangen-Nürnberg

Vorsitzender des Prüfungsorgans:	Prof. Dr. Georg Kreimer
Gutachter:	Prof. Dr. Jürgen Neubauer
	Prof. Dr. Rainer Hock
Tag der mündlichen Prüfung:	14.08.2020

Abstract

This dissertation offers new concepts for the mineralogical characterization of hydrothermally synthesized tobermorite and commercial autoclaved aerated concrete (AAC). The applied key methods include X-ray powder diffraction (XRD) combined with Rietveld refinement, scanning electron microscopy (SEM) and differential thermal analysis (DTA). 11 Å tobermorite was synthesized from various compounds characterized by different dosages of metakaolin. The Al^{3+} incorporation into the lattice of tobermorite and the formation of katoite are verified by XRD analysis. The impact of Al^{3+} incorporation on the microstructural properties of tobermorite is determined by the change of lattice parameters and by use of a Rietveld-compatible approach to anisotropic peak broadening due to domain morphology. Any change of the Al_2O_3 dosage in the raw mix affected the lattice parameters of tobermorite, while the domain morphology was only altered within a small range of Al_2O_3 contents. The disadvantages of SEM analysis of tobermorite in AAC compared to XRD analysis are presented in detail. Regardless of the chemical composition, the morphology of tobermorite in AAC appeared heterogeneous and could only be observed clearly in the pores and pore surfaces. Investigation of the effect of sulfate dosage on tobermorite in AAC revealed that in most samples all of the sulfate was present in anhydrite and did consequently not affect the structure of tobermorite. Finally, improvements of the monitoring of the phase development during the entire production process of AAC are presented. Especially the tracking and characterization of portlandite and tobermorite during AAC manufacturing are refined.

Kurzfassung

Im Rahmen dieser Dissertation wurden neue Herangehensweisen zur Charakterisierung von hydrothermal synthetisiertem Tobermorit und großtechnisch hergestelltem Porenbeton ausgerarbeitet. Die dabei wichtigsten angwandten Analysemethoden umfassen Rötgenbeugungsanalyse (XRD) kombiniert mit Rietveld-Verfeinerung, Rasterelektronenmikroskopie (REM) und Differenz-Thermoanalyse (DTA). 11 Å-Tobermorit wurde aus verschiedenen Anteilen an Metakaolin in der Ausgangsmischung synthetisiert. Der Einbau von Al^{3+} in die Struktur von Tobermorit und die Bildung von Katoit wurden mittels XRD untersucht. Die Auswirkungen des Einbaus auf strukturelle Eigenschaften von Tobermorit wurden anhand der veränderlichen Gitterparameter und anhand einer mit der Rietveld-Analyse kombinierten Methode zur Berücksichtigung der anisotropen Relflexverbreiterung erfasst. Der Ursprung der Reflexverbreiterung liegt dabei in der Morphologie kohärent streuender Domänen. Während jegliche Veränderungen des Al_2O_3-Gehalts in der Ausgangsmischung einen Einfluss auf die Gitterparameter zeigten, wurden Auswirkungen auf die Domänen-Morphologie nur innerhalb eines geringen Bereichs von Al_2O_3-Gehalten beobachtet. Die Problematiken bei der REM-Analyse im Vergleich zur XRD-Analyse von Tobermorit in Porenbeton werden genauer veranschaulicht. Unabhängig von der chemischen Zusammensetzung des Porenbetons zeigte sich bei der REM-Analyse eine sehr heterogene Morphologie der Tobermorit-Kristalle, die allerdings nur in den Poren und an Porenoberflächen beobachtet werden konnte. Die Untersuchung der Auswirkungen des Sulfatgehalts auf die Bildung von Tobermorit in Porenbeton ergab, dass das gesamte Sulfat im System in Form von Anhydrit vorliegt und somit kein Einfluss auf die Struktur von Tobermorit besteht. Weiterhin werden Verbesserungen zur Erfassung des Phasenbestands aufgezeigt, die beide der grundlegenden Fertigungsschritte bei der Herstellung von Porenbeton betreffen. Dabei stehen die Quantifizierung und Charakterisierung der Bildung von Portlandit und Tobermorit im Vordergrund.

List of papers and declaration of author contribution

This thesis is based on the following three publications:

Hydrothermal synthesis of 11 Å tobermorite – Effect of adding metakaolin to the basic compound

Schreiner, J., Goetz-Neunhoeffer, F., Neubauer, J., Jansen, D., 2020. Hydrothermal synthesis of 11 Å tobermorite – Effect of adding metakaolin to the basic compound. Applied Clay Science **185**, https://doi.org/10.1016/j.clay.2019.105432

This publication was in principle written by J. Schreiner in discussion with F. Goetz-Neunhoeffer, J. Neubauer and D. Jansen. J. Schreiner conceptualized the experiments and made all calculations that were needed for the aimed composition of compounds. J. Schreiner conducted all sample preparations including the hydrothermal syntheses. J. Schreiner evaluated XRD experiments and created the tables and figures included in the publication after consultation with F. Goetz-Neunhoeffer, J. Neubauer and D. Jansen.

Advanced Rietveld refinement and SEM analysis of tobermorite in chemically diverse autoclaved aerated concrete

Schreiner, J., Goetz-Neunhoeffer, F., Neubauer, J., Volkmann, S., Bergold, S., Webler, R., Jansen, D., 2019. Advanced Rietveld refinement and SEM analysis of tobermorite in chemically diverse autoclaved aerated concrete. Powder Diffraction **34**, 143–150. https://doi.org/10.1017/s0885715619000149

This publication was basically written by J. Schreiner in discussion with F. Goetz-Neunhoeffer, J. Neubauer, D. Jansen, S. Bergold, R. Webler and S. Volkmann. J. Schreiner conducted and evaluated all XRD experiments. R. Webler, S. Bergold and S. Volkmann performed SEM analysis and the method section for SEM analysis was written by R. Webler and S.

Bergold accordingly. Raw SEM figures were provided by R. Webler and S. Bergold. All final figures included in the publication were compiled and created by J. Schreiner.

New analytical possibilities for monitoring the phase development during the production of autoclaved aerated concrete

Schreiner, J., Jansen, D., Ectors, D., Goetz-Neunhoeffer, F., Neubauer, J., Volkmann, S., 2018. New analytical possibilities for monitoring the phase development during the production of autoclaved aerated concrete. Cement and Concrete Research **107**, 247–252. https://doi.org/10.1016/j.cemconres.2018.02.028

The results and discussion of this paper were mainly written by J. Schreiner in discussion with F. Goetz-Neunhoeffer, J. Neubauer, D. Jansen, D. Ectors and S. Volkmann. D. Jansen and J. Schreiner both created the introduction and experimental sections. J. Schreiner conducted and evaluated XRD and laser scattering experiments and created most of the figures included in the publication. GADDS-system experiments were conducted by D. Jansen and D. Ectors. Figure 7 was created by D. Jansen accordingly. Sample preparations for all experiments except for the GADDS-system were performed by J. Schreiner.

Contents

Abstract I

Kurzfassung II

List of papers and declaration of author contribution III

1 Introduction 1

2 State of research 3

2.1 Mineralogical characteristics of 11 Å tobermorite . . . 3

2.1.1 Tobermorite structure . . . 3

2.1.2 Synthesis of stoichiometric 11 Å tobermorite . . . 5

2.1.3 Substitutions in the lattice of tobermorite . . . 6

2.2 Characterization of autoclaved aerated concrete . . . 7

2.2.1 SEM analysis . . . 8

2.2.2 XRD analysis . . . 10

3 Main results 12

3.1 Hydrothermal synthesis of tobermorite on a laboratory scale - application of two types of metakaolin . . . 13

3.2 Structural properties of tobermorite in AAC - SEM versus XRD analysis . 17

3.3 Improved monitoring of the phase development during the production of AAC . . . 19

4 Conclusions 23

5 References 25

6 Publications 30

6.1 Hydrothermal synthesis of 11 Å tobermorite – Effect of adding metakaolin to the basic compound . . . 30

6.2 Advanced Rietveld refinement and SEM analysis of tobermorite in chemically diverse autoclaved aerated concrete . . . 37

6.3 New analytical possibilities for monitoring the phase development during the production of autoclaved aerated concrete . . . 38

7 Acknowledgement 45

1 Introduction

Tobermorite is a naturally occurring calcium silicate hydrate forming under hydrothermal conditions. It is mainly found in calcium-rich metamorphic rocks such as marble and skarn [1]. In 1880 the mineral was described for the first time by Heddle at its type locality of Tobermory (Scotland) [2, 3]. The tobermorite supergroup includes various related mineral species characterized by basal spacings of 9, 11 and 14 Å and different sub-cell symmetries [4].
Besides its occurrence in rocks, tobermorite is a major well-crystalline mineral phase present in commercial masonry units such as sand-lime bricks and autoclaved aerated concrete (AAC). Commonly, in these products the 11 Å species with the chemical formula $Ca_5Si_6O_{16}(OH)_2 \cdot 4\,H_2O$ and orthorhombic sub-cell symmetry is present. In equivalence to the crystallization of 11 Å tobermorite in a geological environment, hydrothermal treatment of masonry units triggers its formation during production. Thermal and mechanical properties of these products depend on the microstructure and mineralogical phase composition. For this reason, the investigation of the crystallization process and the morphology of tobermorite[1] crystals have been subject of numerous studies [5, 6, 7]. Conventionally, scanning electron microscopy (SEM) analysis is the most applied method for this purpose [8, 9, 10, 11]. In addition, poorly-crystalline C-S-H in hydrating cement pastes was structurally derived from a tobermorite species [12]. Apart from construction technology, tobermorite has found several applications due to its ion exchange capacity [13] - for instance in wastewater treatment or radioactive waste management [14, 15].

AAC is an established masonry material due to its thermally insulating capacities combined with low densities of 275 - 750 kg/m^3 [16] and sufficient compressive strength for construction. The fabrication is divided in two fundamental process stages and was exemplarily portrayed in the work of Schober [17]. The major materials needed for production are quartz sand, burnt lime, cement, a sulfate source and water. Compared to foamed concrete, the pores in AAC are generated based on the release of hydrogen gas due to a chemical reaction of aluminum powder triggered by an alkaline environment during the cement hydration [17, 18]. The first production step includes the green body hydration as well as the generation of pores, which endure the hydrothermal curing and are present

[1] Unless otherwise specified, "tobermorite" in the following always refers to the 11 Å species.

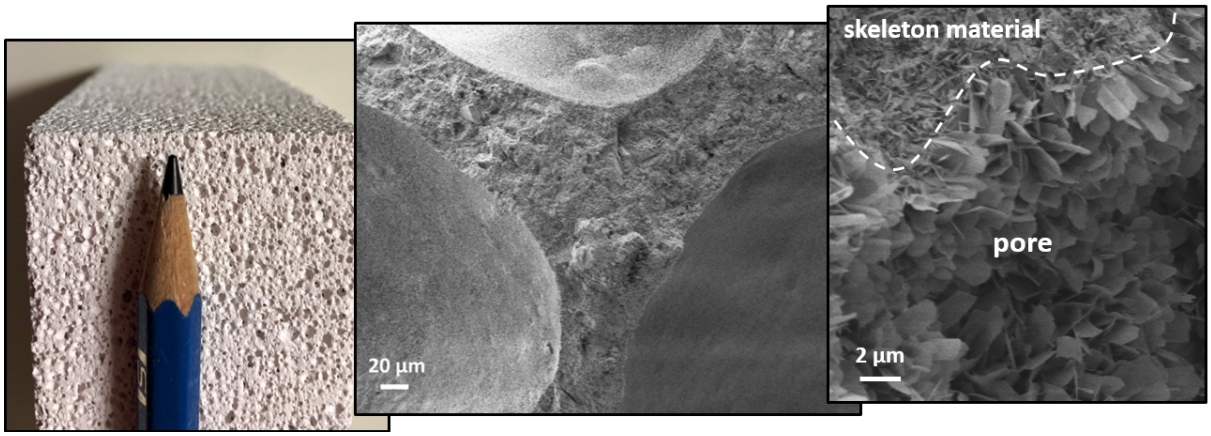

Figure 1.1: Porous structure of autoclaved aerated concrete.

in the final product (Figure 1.1). During the second production step the green cakes are treated hydrothermally under saturated steam pressure in order to gain compressive strength. A shift of the pore size distribution during the autoclaving process was reported by Mitsuda et al. [10].

Generally, the rather complex phase development during the production process of AAC is insufficiently considered. Established AAC products are very often the result of purely empirical and time-consuming test series. Therefore, a better understanding and monitoring of the phase development is the preferable way. This thesis is intended to demonstrate advanced analytical methods for the characterization of 11 Å tobermorite in both, lab-scale samples and commercial AAC. The majority of innovations are gained from X-ray diffraction (XRD) and an approach to fit anisotropic peak broadening [19] compatible with Rietveld refinement [20]. The suitability of SEM analysis in this context is discussed. Moreover, effects of changes in the chemical composition in the starting compound are investigated. Finally, the new analytical possibilities are applied to the entire production process of AAC.

2 State of research

2.1 Mineralogical characteristics of 11 Å tobermorite

2.1.1 Tobermorite structure

The orthorhombic tobermorite structure basically consists of sevenfold coordinated [21] calcium polyhedral layers and silicate tetrahedral chains (Figure 2.1) [3]. Running along *b*, two pairing tetrahedra centered by Si cations are connected by another Si-centered bridging tetrahedron [3].

Apart from the undisputed layered structure and the wollastonite-like chains, several approaches have coexisted regarding the possible space groups and the location of the remaining calcium cations and water molecules in the lattice of 11 Å tobermorite [3, 21, 22, 23]. However, Biagioni et al. presented a new nomenclature for the tobermorite supergroup including very precise structures [4]. Oxygen atoms, hydroxyl groups and water molecules are located at the apical sites of the calcium polyhedra. The Si-centered bridging tetrahedra of the wollastonite-like chains share the oxygen and hydroxyl groups with the calcium polyhedra. Merlino et al. and Biagioni et al. stated that additional water molecules and cations are located in structural cavities running along *b* [3, 4]. According to Merlino et al. and Bonaccorsi et al. the content of these zeolitic cavities is the determining factor for the resulting tobermorite species [3, 24]. The additional cation in the interlayer is primarily calcium, so that there is a variability of calcium content between 4 and 5 atoms per formula unit [4]. 11 Å tobermorite is characterized by the calcium-rich endmember of this series [4]. The interlayer calcium is then sixfold-coordinated by framework oxygen atoms. The amount of interlayer water molecules determine the degree of hydration and the basal spacing of the resulting tobermorite species [24]. The reader is referred to a well-specified categorization of all tobermorite polytypes provided in the publications by Merlino et al., Bonaccorsi et al. and Biagioni et al. [3, 4, 24, 25].

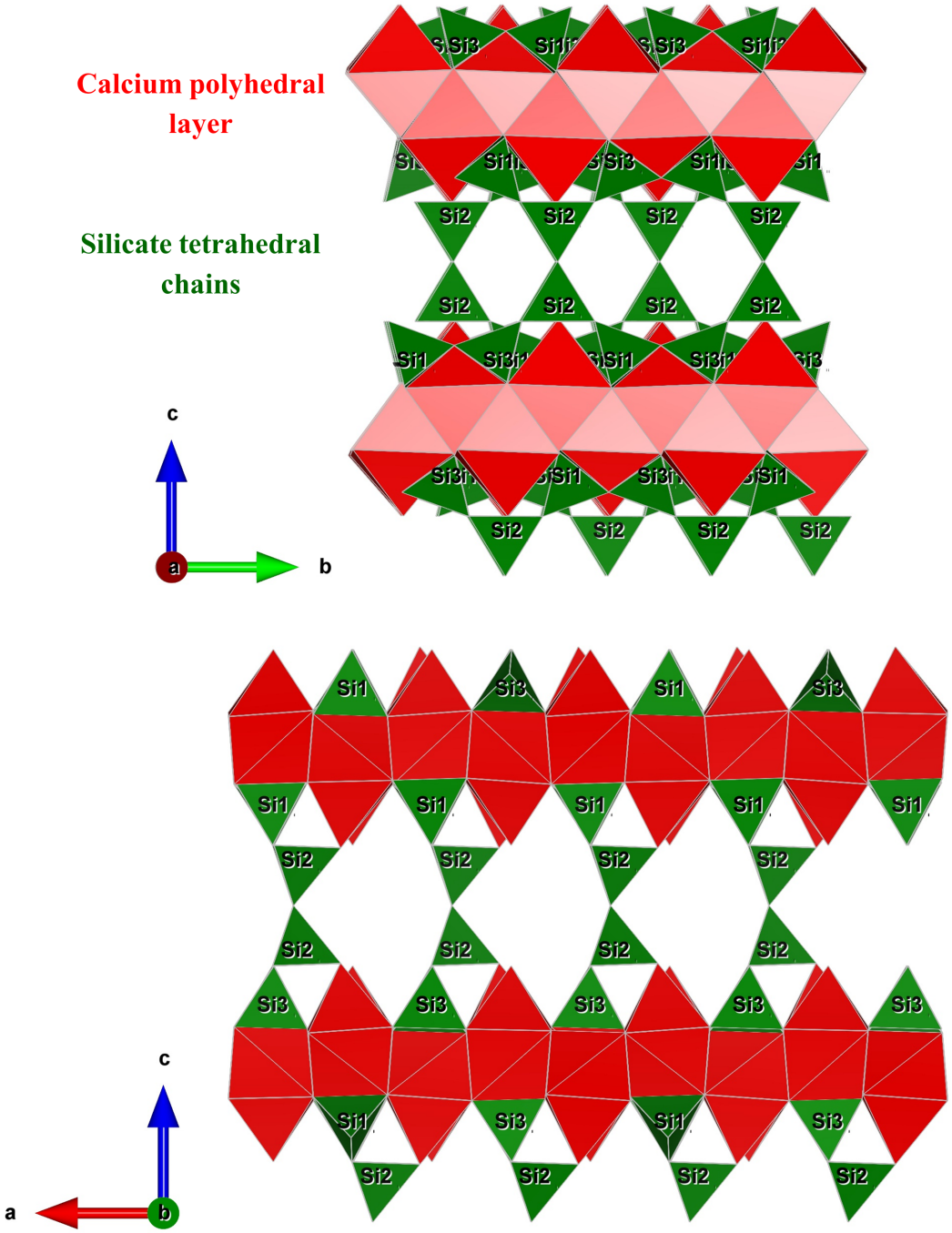

Figure 2.1: Calcium polyhedral layers and silicate tetrahedral chains in 11 Å tobermorite structure according to Merlino et al. [3]. Si1 and Si3 = pairing tetrahedra, Si2 = bridging tetrahedra. Interlayer water molecules and cations are not shown. Figure created with *VESTA 3.1.6* [26].

2.1.2 Synthesis of stoichiometric 11 Å tobermorite

The starting materials required for the hydrothermal synthesis of stoichiometric tobermorite are quartz flour or a different silica source, calcium oxide or calcium hydroxide and deionized water [7, 22]. In accordance with the chemical formula, the starting mix appropriately conforms to a Ca/Si molar ratio of about 0.8 [9, 27].
After preparing the slurry, a distinct temperature setting of 170-180 °C, autogenous saturated steam pressure (1–1.2 MPa) and a curing time of 12 h were recommended [5, 7, 28]. Consequently, an elevated water-to-solid ratio [7, 23] in the starting mix and high overall water content are required in order to ensure a saturated steam atmosphere in the laboratory autoclave. Qu et al. showed that shorter curing times led to a lower reaction turnover [6]. According to Šiaučiūnas & Baltakys at prolonged curing duration the formation of xonotlite ($Ca_6Si_6O_{17}(OH)_2$) was favored [7]. It has been reported that the surface area and solubility of all raw materials have an effect on the reaction time and reaction products [7, 9, 29]. For instance, gyrolite formation was triggered by highly soluble amorphous SiO_2 in a study by Šiaučiūnas & Baltakys [7]. El-Hemaly et al. showed that when amorphous type of silica was used, the formation of C-S-H was accelerated but the subsequent conversion to tobermorite was slowed down [22].
The simplified hydrothermal reaction path (equation 2.1) [10, 27, 30] for the formation of stoichiometric tobermorite was described as follows. Depending on the surface area of raw materials, the dissolution of $Ca(OH)_2$ and SiO_2 in the hydrothermal environment initially leads to the formation of a C-S-H gel, which is characterized by poor structural order in c direction [22, 27]. The Ca/Si molar ratio in this precursor is variable [30]. The hydrothermal reaction proceeds and the C-S-H gel transforms into tobermorite but with a more particular Ca/Si ratio of approximately 0.83. The Ca/Si ratio decreases in this step, as further SiO_2 is dissolved and supplied for reaction [10]. Within this step, periodicity in c direction increases and the calcium polyhedral layers and silicate chains gain more structural order as reported by Shaw et al. [27].

$$xCa(OH)_2 + ySiO_2 + H_2O \implies C\text{-}S\text{-}H\ gel \implies C\text{-}S\text{-}H\ gel + zSiO_2 \implies tobermorite \tag{2.1}$$

Commonly, pure phase synthesis of tobermorite is hardly attainable and some minor phases and amorphous content are frequently present in samples after hydrothermal curing. Common additional phases occurring in this system include calcite, quartz, xonotlite, scawtite and poorly crystalline C-S-H with varying Ca/Si composition [7, 9, 31].
In most studies autoclaved samples were dried at 60 - 100 °C [6, 29] and ground prior

to further analyses. Synthesized samples are commonly investigated by means of thermogravimetric analysis (TGA) combined with differential thermal analysis (DTA), SEM analysis and X-ray diffraction. For estimation of the chemical purity of tobermorite, usually the basal spacing of 11.3 Å is verified by XRD analysis, as substitutions such as Al^{3+} incorporation would reflect in it [15, 28]. Moreover, according to Mostafa et al. and Qu et al., stoichiometric tobermorite showed plate-like morphology in SEM images [6, 32].

2.1.3 Substitutions in the lattice of tobermorite

The incorporation of foreign ions into the lattice of tobermorite has been investigated in two major respects. In the first case, the substitutions occur during the application of previously synthesized tobermorite. The potentials of these substitutions were exemplarily highlighted in chapter 1 [14, 15]. In the second case, the substitutions occur during the hydrothermal formation of tobermorite. Whenever a basic compound includes chemical components apart from calcareous materials and silica, substitution in the lattice of tobermorite is likely to happen during the hydrothermal reaction. Biagioni et al. stated that Al-free natural tobermorite is extremely rare [4].
Supplementary cementitous materials (SCMs) are established components in various applications - equally in AAC production. Merchantable SCMs are usually limited to well available materials, so that only distinct foreign ions are supplied in a considerable scale. Calcined clays, diatomite, blast furnace slag and especially metakaolin are amongst the most frequent materials for this purpose [31, 33, 34, 35]. They are, in turn, characterized by a specific chemical composition. These raw materials supply primarily aluminum and alkali metal cations. In addition, the presence of sulfate ions in the system has been considered by some authors, since sulfate is a component in most composites for construction [32, 36].
Sakiyama & Mitsuda and Rios et al. successfully synthesized Al-substituted tobermorite by applying different amounts of kaolinite and metakaolin [5, 23]. The incorporation of Al^{3+} into the lattice of tobermorite resulted in lath-like crystals[1] observed by SEM analysis. At a higher Al^{3+} dosage the formation of katoite was reported. Skawinska et al. investigated various halloysite contents in the initial mix [34]. They confirmed katoite formation caused by increased supply of Al^{3+}. The substitution of Si^{4+} by Al^{3+} in the tetrahedral chains ranges to a possible 1/6 substitution of the tetrahedral sites reaching an Al content up to 1 Al atom per formula unit [4]. Merlino et al. explained that this mainly occurred in the bridging tetrahedron and for charge balance additional $(OH)^-$ substituted O^{2-} in one site [3]. This leads to an increase of the basal spacing and lattice parameter *c*,

[1]The terminology of observed crystalline particles is addressed in subsection 2.2.2.

which was observed in several studies [15, 28, 37]. In a different publication by Jackson et al. the incorporation of additional Na^+ or K^+ for charge balance was suggested [38]. Matekonis et al. stated that in this case tobermorite showed anomalous thermal behavior [29]. Furthermore, ^{29}Si NMR measurements revealed that the substitution by Al^{3+} led to an increase of the chain length in b direction [38, 39]. Klimesch & Ray performed thermal analysis of Al-free and Al-substituted tobermorites [40]. They reported that in the case of Al^{3+} incorporation, the conversion of 9.3 Å tobermorite into β-wollastonite required a higher temperature. This observation is discussed later in this thesis (section 3.1). Qu et al. performed XRD analysis and considered relative intensity broadening of Al-substituted tobermorite reflections in order to estimate the crystallinity [6]. However, the broadening was not measured and evaluated. The present thesis provides extensive insights into the evaluation of the peak broadening of tobermorite depending on the supply of Al^{3+} (section 3.1 and section 3.2).
According to Mostafa et al. substitution by $(SO_4)^{2-}$ in the lattice of tobermorite led to basal imperfection [32]. Their study was mainly based on XRD analysis and FTIR spectroscopy. It was suggested that charge balance was achieved by substitution of $(SO_4)^{2-}$ and $2\,(OH)^-$ for $(SiO_4)^{4-}$. Moreover, the transformation of C-S-H gel into tobermorite was accelerated. The sulfate-substituted tobermorite showed leafy crystals in SEM images. By contrast, Sauman & Valtr stated that the morphology of sulfate-substituted tobermorite did not differ substantially from the morphology of stoichiometric tobermorite crystals [41]. Instead, anhydrite formation was observed by means of XRD analysis. In section 3.2 of this thesis a new perspective on this discussion is provided.

2.2 Characterization of autoclaved aerated concrete

Supplied materials for AAC fabrication are transforming continuously during the production process, which is displayed in Figure 2.2 [42]. It can be seen that the phase transitions before autoclaving remind of ordinary portland cement (OPC) hydration [43]. The following main reactions run during the hydration before autoclaving [10, 12, 17].

$$CaO + H_2O \implies Ca(OH)_2 \tag{2.2}$$

$$Ca_3SiO_5 + 3.9H_2O \implies C_{1.7}SH_{2.6} + 1.3Ca(OH)_2 \tag{2.3}$$

$$Ca_3Al_2O_6 + 3CaSO_4 + 32H_2O \implies Ca_6Al_2(OH)_{12}(SO_4)_3 \cdot 26H_2O \tag{2.4}$$

This process step is finished when the generation of pores along with simultaneous expansion is completed and sufficient strength for wire cutting has developed through hydration.

The reaction of aluminum powder does not only lead to the formation of hydrogen gas but to very low amounts of different modifications of aluminum hydroxide [17]. However, it can be seen that none of the hydrate phases forming during the green cake setting endure the autoclaving process. Only quartz does partially not react and is consequently present in the final product. After transforming into ettringite and later AFm phases, initially supplied anhydrite recrystallizes during the hydrothermal treatment. A multi-step reaction sequence of C-S-H, portlandite and further intermediate hydration products leads to the crystallization of tobermorite. The reader is referred to the comprehensive study of Schober for a more detailed presentation [17]. Further supply of dissolved silica at hydrothermal conditions contributes to the formation of tobermorite in the manner outlined in equation 2.1. Clearly, tobermorite is the major mineral phase present after autoclaving and is therefore the main focus of research. In the following subsections 2.2.1 and 2.2.2 the state of knowledge concerning the characterization of AAC by means of SEM analysis and XRD analysis is provided.

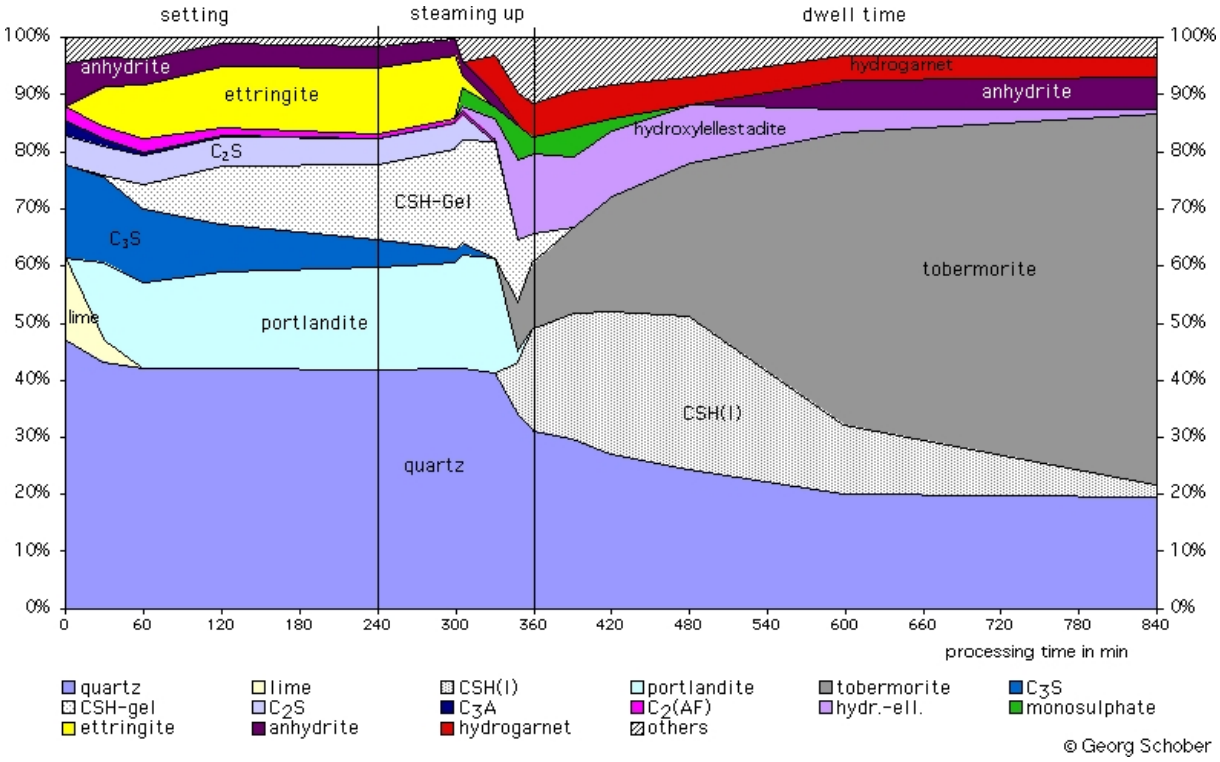

Figure 2.2: Exemplary phase development during the entire production process of AAC. Figure adopted with permission from Schober [42].

2.2.1 SEM analysis

At first sight AAC has rather favorable properties compared to hydrated Portland cement when it comes to SEM analysis. Due to the hydrothermal treatment several phases such

as tobermorite show better crystallinity. In addition, the hardly evitable effects of damage to poorly crystalline phases and removal of water are not as significant in the case of AAC. This is why environmental scanning electronic microscopy (ESEM) was suggested in order to investigate hydrated Portland cement after early hydration [44, 45]. However, while hydrated OPC is a reasonably homogeneous material, AAC shows heterogeneity due to the porous structure (Figure 1.1).
As reported in subsection 2.1.3, several authors investigated the morphology of tobermorite in AAC in order to verify the influence of foreign ions supplied by SCMs and estimate their effect on the thermal and mechanical properties. Well crystallized tobermorite often shows a house-of-cards structure in AAC (Figure 2.3), which was observed in numerous studies [46, 47, 48].

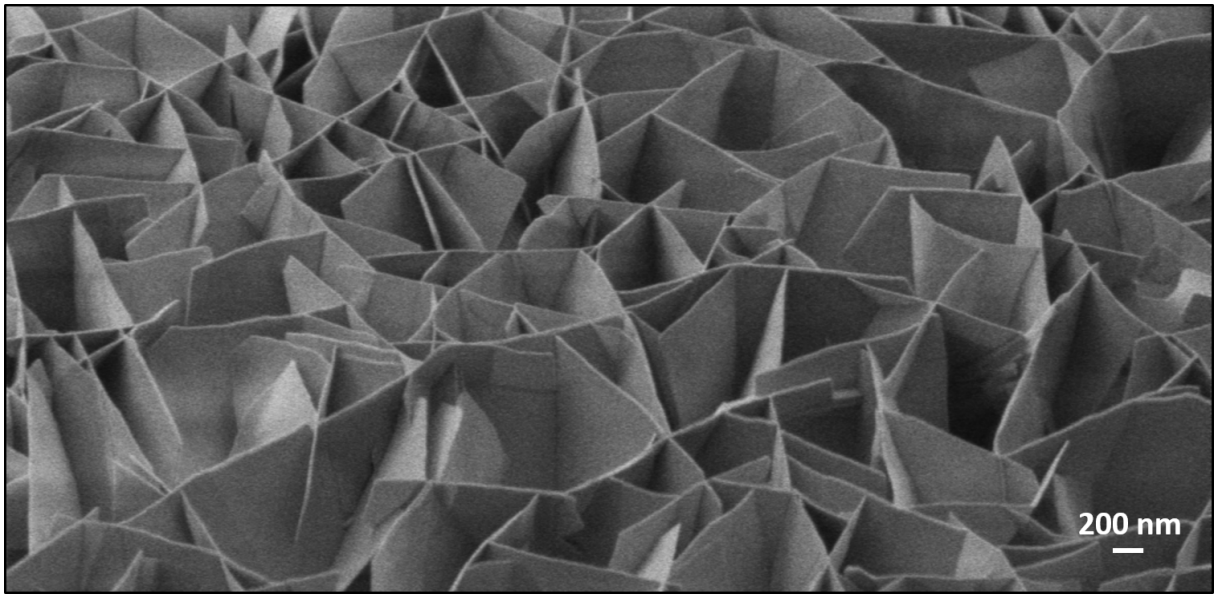

Figure 2.3: House-of-cards appearance of tobermorite crystals in AAC.

Wongkeo & Chaipanich stated that the application of coal bottom ash for partial replacement of cement in the starting compound resulted in a change of plate-like to lath-like morphology of tobermorite crystals [49]. Equally, thin lath-like plates of tobermorite were observed by Różycka et al. in samples prepared from perlite waste [50]. Venhodová et al. investigated AAC samples prepared from mixes including fly ash and $Al(OH)_3$ and confirmed the elongated shape of Al-incorporated tobermorite [8]. In these studies the fraction of aluminum ions was increased by adding the respective SCM. An effect on the morphology of tobermorite was respectively reported, which conforms to the conclusions made by different authors in subsection 2.1.3. Nevertheless, the heterogeneity of AAC samples in SEM images was barely addressed in all of these examples. By contrast, Mitsuda et al. differentiated between macropores and micropores in their SEM images of industrially manufactured AAC [10]. Huang et al. separately analyzed walls and pores in

their samples prepared from copper tailings and blast furnace slag [48]. The wall sections appeared dense, while in pores platy tobermorite and long-strip shaped anhydrite was observed. Only the tobermorite crystals in the pores showed the previously described house-of-cards structure. As is evident from these published results, there is a lack of clarity about the meaning and informative value of observations made in AAC samples by SEM analysis. In the main results of this present thesis (section 3.2) a substantiated assessment of this circumstance is given.

2.2.2 XRD analysis

While SEM analysis of AAC is majorly performed in order to characterize the crystallinity and morphology of tobermorite, XRD analysis is mainly applied in order to assess the overall phase composition. Apart from the phases shown in Figure 2.2, additional calcite, feldspar, mica, gypsum and bassanite occur frequently in AAC depending on the mineralogical composition of the used raw materials. Frequently, minor phases are unreacted residual components of raw materials such as sericite in the publication of Isu et al. [51] or phlogopite in the study of Huang et al., who applied skarn-type copper tailings for AAC preparation [48]. Prolonged curing duration resulted in minor quantities of xonotlite in the study by Mitsuda et al. [10].
Mainly qualitative phase contents have been determined based on XRD in studies dealing with the mineralogy of AAC. A clear recognition of amorphous content in AAC along with the crystalline phases has been barely addressed and discussed. Relative quantities were determined by Matsui et al. by plotting normalized intensities [28]. They estimated the quantity of C-S-H gel by regarding the integrated intensity of the assumed tobermorite precursor in a distinct section of the XRD pattern. Coming in agreement with the authors cited in subsection 2.1.3, increased d spacing along c in Al-substituted tobermorite was reported in the same study. Venhodová et al. performed XRD analysis of AAC samples in their publication previously addressed in subsection 2.2.1 [8]. They compared relative intensities of tobermorite in their samples, but no absolute quantities of the phases were calculated either. Mitsuda et al. applied an internal standard method in order to quantify unreacted quartz in their AAC samples [10].
More recently, Ectors proposed a promising method for the tracking of portlandite formation during the green cake hydration [52]. By applying a Rietveld compatible approach for *TOPAS 5.0* (Bruker AXS) to fit anisotropic peak broadening due to domain morphology [19], two generations of portlandite could be refined separately and assigned to the hydration of calcium oxide and tricalcium silicate, respectively. The key idea behind this approach is that the average domain morphology of a mineral phase in a powder

sample implies certain mineralogical characteristics. The simplified domain morphology can be calculated on the basis of geometrical shapes such as cylinder, ellipsoid or cuboid. Depending on the crystal system and the expected morphology, the geometrical shape can be adjusted accordingly. In the example reported by Ectors, the one generation of portlandite originating from burnt lime hydration showed anisotropic peak broadening - unlike the generation forming from tricalcium silicate hydration. In accordance with the trigonal crystal system, a biaxial cylinder model was applied for the fitting of the anisotropic generation. The operating principle of the approach to fit the anisotropic peak broadening due to domain morphology can be precisely explored by accessing further publications by Ectors et al. [53, 54]. Apart from this benefit, a better fit to the measured data enables a more accurate refinement and quantification of all phases. The two generations of portlandite were additionally quantified by means of an external standard method [55]. The combination of quantitative phase analysis by XRD (QXRD) with the refinement of anisotropic peak broadening is a promising approach in this context - especially in consideration of the fact that phase quantifications in AAC samples have been barely performed ever before. Hence, the application of these methods is the key matter of this present thesis. Especially the potential of the domain morphology analysis of tobermorite is precisely investigated. The terms domain size and domain morphology in this sense refer to the coherently scattering unit measured by XRD analysis. Crystalline particles observed by means of electron microscopy, which are frequently termed grains, crystals or crystallites, are for the most part clusters of coherently scattering domains [56, 57].

3 Main results

This chapter introduces the main results presented in three peer reviewed publications [58, 59, 60] incorporated in chapter 6. The new findings are put in a general context and subsequently they are summarized and discussed in chapter 4. The sections 3.1 and 3.2 deal with the characterization of tobermorite in both, lab-scale samples and AAC samples produced on an industrial scale. In section 3.3 the entire production process of AAC including the hydration before autoclaving is addressed.

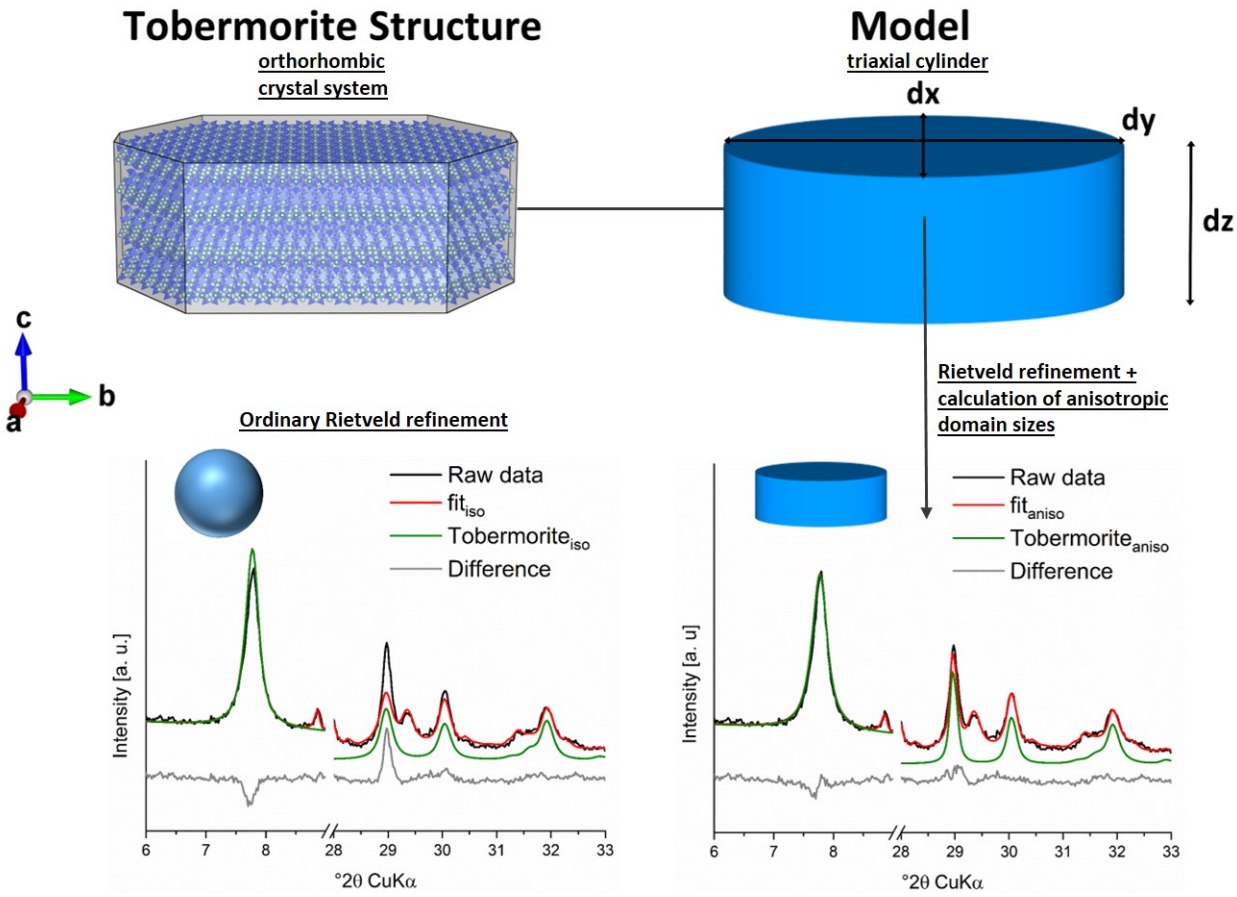

Figure 3.1: Application of a triaxial cylinder model for the calculation of anisotropic domain sizes of tobermorite implemented with Rietveld refinement and influence on the fit compared to ordinary refinement [60].

One particular main result is a key element in each of the following sections. In Figure 3.1 the fit of tobermorite after two Rietveld refinements of different accuracy is shown. In a regular Rietveld refinement, for simplification the coherently scattering units are treated as spherical shapes, as usually only one size value for each mineral phase is calculated. As average domain sizes of a mineral phase in different crystallographic directions are in many cases indeed close to one value, this approximation is often sufficient in order to achieve a satisfactory fit to the measured diffractogram. The crystal system and surrounding conditions during the formation of a mineral phase are significant factors in this context. A misfit at different (hkl) reflections as displayed in Figure 3.1 is an indication of anisotropic peak broadening. Clearly, orthorhombic tobermorite shows anisotropic peak broadening due to its anisotropic domain morphology. For the possible origins of anisotropic peak broadening apart from size broadening, the reader is referred to section 6.1. In accordance with the orthorhombic crystal system, a triaxial model is applied in order to fit the peak broadening [19]. By implementing the macro during the refinement, no longer one but three sizes (x, y and z for respectively a, b and c direction) are calculated. Besides the improved fit, the calculated domain morphology is an additional information extracted from XRD analysis and it is representative for the average value of the phase in the entire sample. In each of the following sections the different benefits regarding this approach are outlined in more detail.

3.1 Hydrothermal synthesis of tobermorite on a laboratory scale - application of two types of metakaolin

This study covers mineralogical properties of tobermorite synthesized from a set of various compounds including different amounts and types of metakaolin [58]. Unlike in sections 3.2 and 3.3, the samples were not aerated before autoclaving and their composition is adjusted to the Ca/Si molar ratio of stoichiometric tobermorite. On the one hand, the reactivity of metakaolin and minor phases at hydrothermal conditions for the possible use in AAC production was investigated. On the other hand, the effects of consequent changes of the bulk chemistry in the basic compound on the mineralogical characteristics of tobermorite such as lattice parameters and domain morphology were analyzed. In addition, for one particular compound the effect of different curing times was explored. While the conventional raw materials for AAC production are rather low-cost resources, metakaolin is a high-priced SCM in this regard. For this reason, besides one comparatively pure commercial metakaolin (MK), a second by-product type of metakaolin (MK_g) was applied

at equivalent dosages. All investigated mix composites and the chemical composition of MK and MK_g are summed up in tables in section 6.1.

In Figure 3.2 the effect of different amounts of the two types of metakaolin on the phase quantities is displayed. Clearly, at moderate dosages of MK and MK_g tobermorite was present in comparable quantities. However, the application of any amount of metakaolin reduced the amount of tobermorite compared to the blank mixture. It can be seen that katoite was present whenever the content of Al_2O_3 in the starting drymix exceeded 2 wt.%, which fits well with the state of knowledge [5, 23]. For the highest possible dosages of the two types of metakaolin ($MK60$ and MK_g60) contrary effects were observed. Application of impure metakaolin (MK_g) led to a considerable amount of tobermorite, while in $MK60$ no tobermorite was present. The high content of Al_2O_3 seems to have hindered the formation of tobermorite. Not all of the Al_2O_3 in MK_g was supplied for reaction, as minor phases such as feldspar remained unreacted, which is shown accurately in the respective publication in section 6.1.

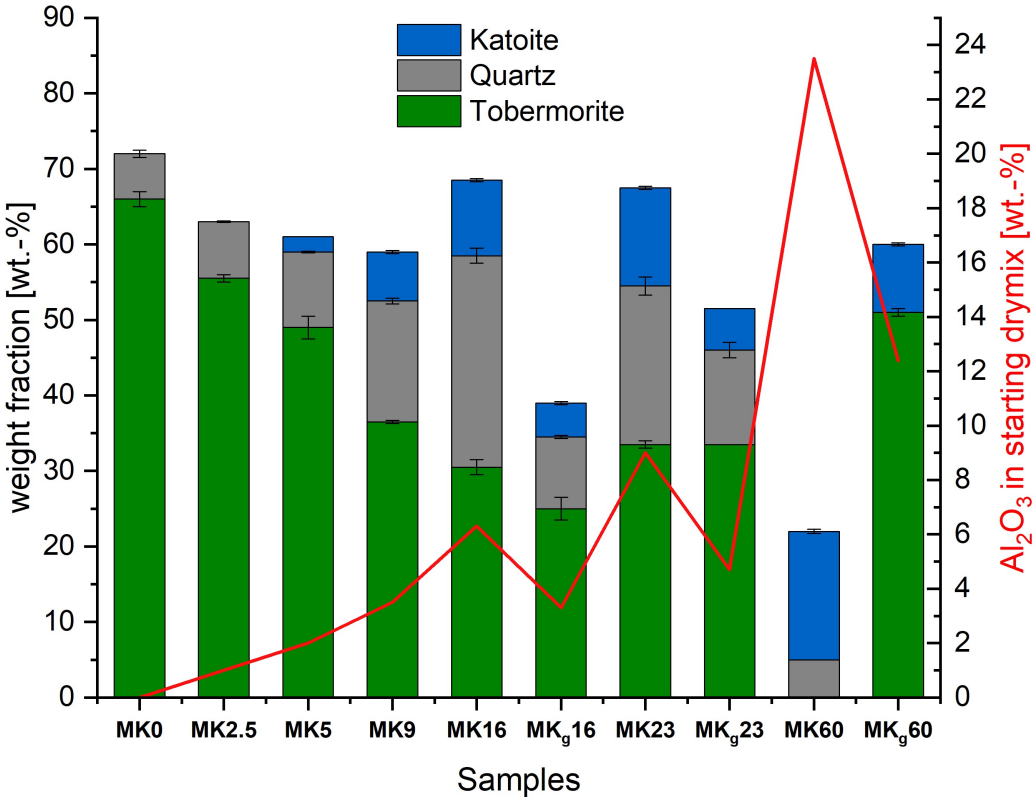

Figure 3.2: Weight fractions of tobermorite, quartz and katoite measured by QXRD analysis and contents of Al_2O_3 in the starting drymix. Amorphous content and minor phases are not shown.

The results of thermal analysis of samples characterized by MK addition in small steps are shown in Figure 3.3. It can be seen that the conversion of 9.3 Å tobermorite into β-

wollastonite depended on the dosage of MK. However, unlike suggested by Klimesch & Ray, there was no effect of lower contents of Al_2O_3 in the drymix [40]. Consequently, the influence of Al^{3+} at low dosages ($MK2.5$ and $MK5$) could not be observed on the basis of this method. Apart from this result, the other signals showed good agreement with the suggested conversion ranges by Klimesch & Ray, as for samples $MK9$ and $MK16$ a clear shift towards higher temperature was measured. However, the role of Al^{3+} incorporation verified by this method is not necessarily conclusive, as additional reactions during the heating experiment involving Al^{3+} are possible. On that basis the observations made by means of DTA would not reflect the amount of Al^{3+} originally incorporated into the structure of 11 Å tobermorite.

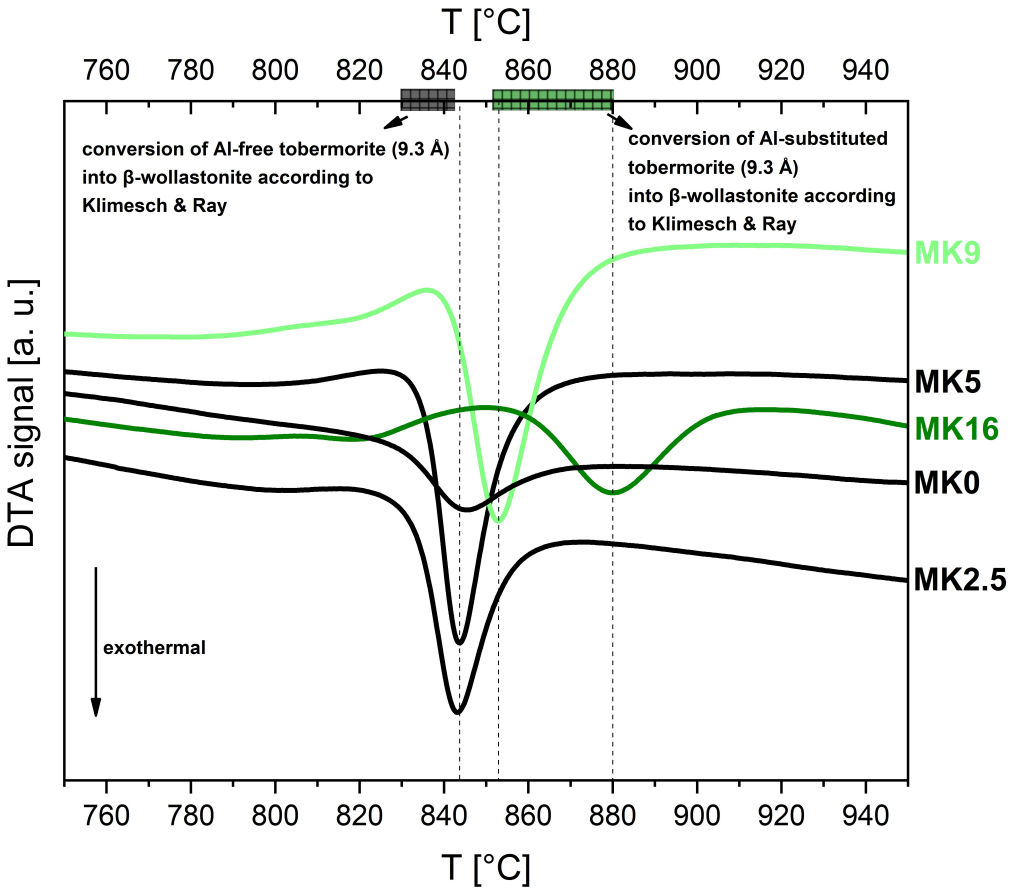

Figure 3.3: Conversion of 9.3 Å tobermorite into β-wollastonite in samples synthesized with various amounts of metakaolin and suggested temperature ranges according to Klimesch & Ray [40].

In accordance with authors referenced in subsection 2.1.3, lattice parameter c of tobermorite increased with elevated dosages of Al_2O_3 in the basic dry mix (Figure 3.4). The impact could be observed for the complete range of samples as displayed in section 6.1, which indicates that a limit of Al^{3+} incorporation was not reached in this study. For comparison, the relative domain morphology is plotted in Figure 3.4. Unlike the DTA

signals, both lattice parameter c and the domain morphology are impacted by very low dosages of Al_2O_3. There is a good accordance of the relation of growth in b direction to a direction and the c parameter. This is valid up to 2.0 wt.% of Al_2O_3 in the starting dry mix. By contrast, more elevated contents of Al_2O_3 did not affect the domain morphology any further, even though the incorporation is verified through the increased c parameter. It follows that the impact of Al^{3+} incorporation on the domain morphology is limited to very low contents, while the impact on lattice parameter c can be tracked throughout the entire examined range of samples. In section 6.1 additional results show that growth in b direction increased with reaction time. These observations are solely based on XRD analysis and offer new benefits for the structural understanding of tobermorite.

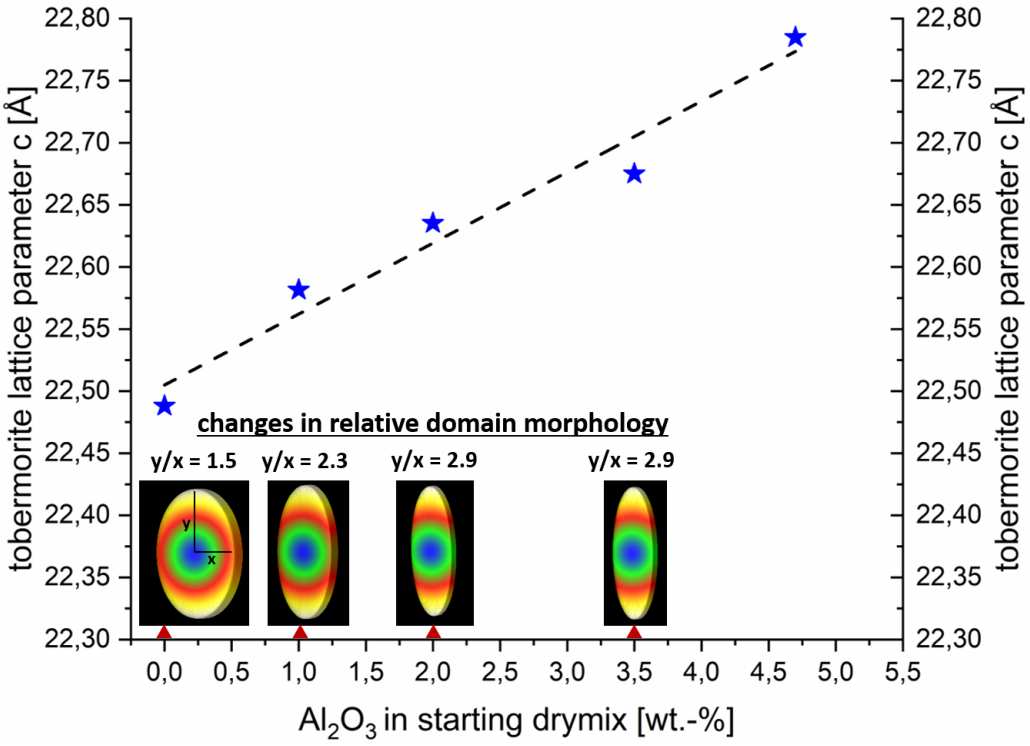

Figure 3.4: Impact of the calculated Al_2O_3 content in the basic dry mix on the lattice parameter c and on the relation of calculated domain sizes of tobermorite in a (x) and b (y) direction.

3.2 Structural properties of tobermorite in AAC - SEM versus XRD analysis

This section and the respective publication [59] mainly deal with the suitability of SEM analysis of tobermorite in AAC. The effects of varying amounts of SO_3 and Al_2O_3 in the dry mix on structural properties of tobermorite are discussed based on XRD analysis.
As shown in subsection 2.2.1 and Figure 2.3, tobermorite often shows a house-of-cards structure in AAC samples. This property has been considered to be relevant for the thermal and mechanical properties of AAC (subsection 2.2.1). However, SEM analysis within this study revealed that this type of appearance is mainly found in the pores and pore surfaces (Figure 3.5). This finding comes in agreement with the observations made by Huang et al. [48]. In the solid skeleton of the dense AAC material, neither the morphology, nor the house-of-cards structure could be observed properly, which can be seen very clearly in additional micrographs provided in section 6.2. It should be considered that the major amount of tobermorite by weight is located in the dense material and not at the pore surfaces. In this way, these findings are clear disadvantages coming along with only SEM analysis of AAC, as representative results can hardly be obtained.

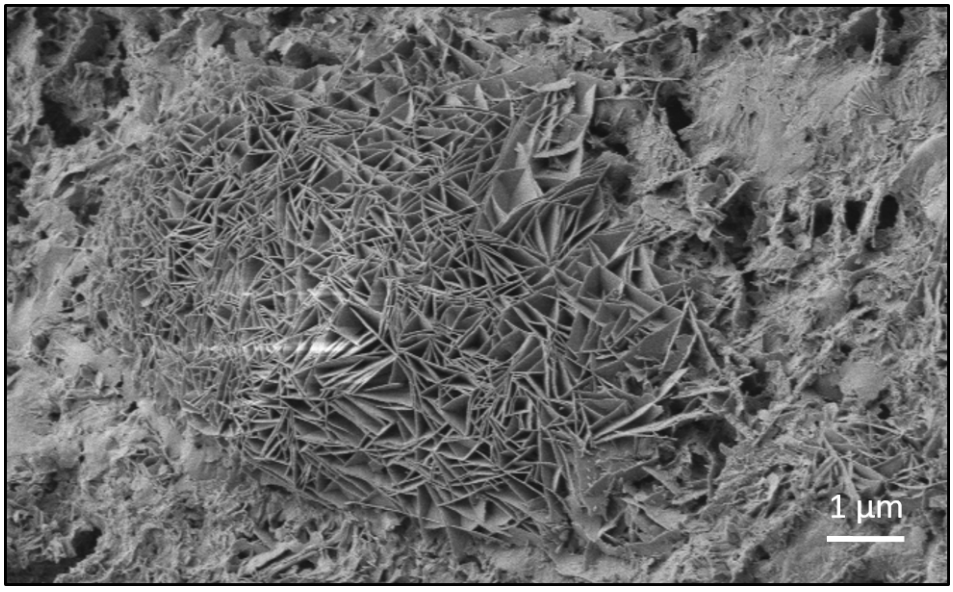

Figure 3.5: House-of-cards structure of tobermorite in a pore surrounded by dense material.

Moreover, several authors in subsection 2.2.1 justified the morphology of tobermorite with the incorporation of foreign ions. Al-substituted tobermorite showed lath-like morphology, whereas Al-free tobermorite showed rather plate-like morphology [6, 32, 49]. However, the present investigation revealed that independent of Al_2O_3 content in the raw mix, there

is always heterogeneity regarding the morphology of tobermorite. In Figure 3.6 plate-like and lath-like morphology of tobermorite in AAC observed in two statistical, chemically various samples are displayed. This result supports the previous assumption that the observations made by SEM analysis of tobermorite in AAC strongly depend on what part of the sample is selected. Yet again, no clear observations could be made that were representative for the entire sample.

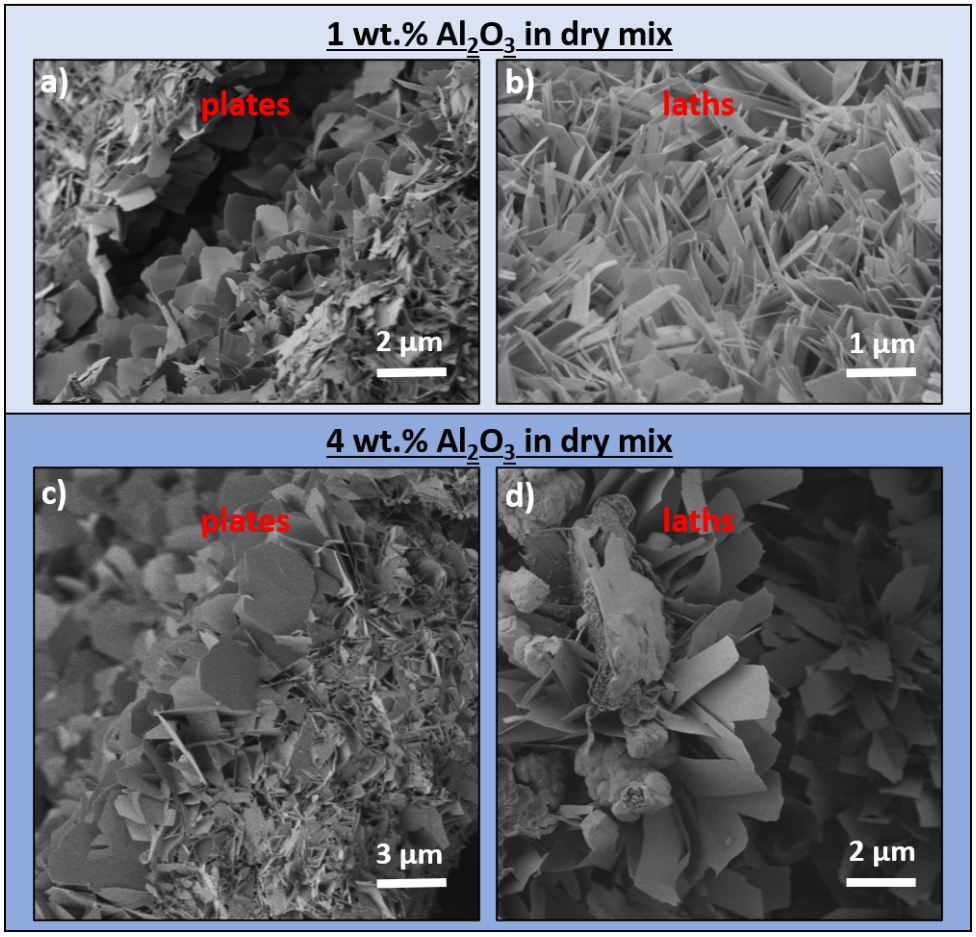

Figure 3.6: Heterogeneous morphology of tobermorite (plate-like in a and c, lath-like in b and d) in two AAC samples characterized by different Al_2O_3 contents in the raw mix.

The effects of Al^{3+} on the domain morphology of tobermorite were measured and evaluated in a similar manner as in section 6.1 and the results could be confirmed. The relative domain growth in b direction was increased by Al^{3+} incorporation in both studies [58, 59]. Moreover, lattice parameter c was increased with Al^{3+} incorporation, which can be seen more accurately in section 6.2. Unlike SEM analysis, XRD analysis allowed clear conclusions whenever structural properties of Al-substituted tobermorite were affected. Instead of a local observation as made with SEM, representative and statistical results were obtained. The reader is referred to section 6.1 and section 6.2 for further results and

more specific conclusions.
In addition, the effect of various amounts of sulfate in the raw mix was analyzed. Unlike in the case of different dosages of Al^{3+}, neither the domain morphology nor the lattice parameters of tobermorite were affected by the SO_3 content in the dry mix. In Figure 3.7 these observations and additionally the amounts of anhydrite measured by QXRD are shown. As the amount of available SO_3 in the dry mix is known, the maximum possible amount of anhydrite could be calculated for each of the samples in focus. Obviously, the measured amounts of anhydrite are either equal or slightly higher compared to the expected quantities. This result leads to the assumption that all of the available sulfate is transformed into anhydrite, so that no more sulfate could be incorporated into the structure of tobermorite. The over-estimation of anhydrite in some of the samples can be explained due to the inaccuracy of the quantification method. The present results rather match with the suggestions by Sauman & Valtr [41], as in their study no effect of sulfate on the structure of tobermorite was observed either.

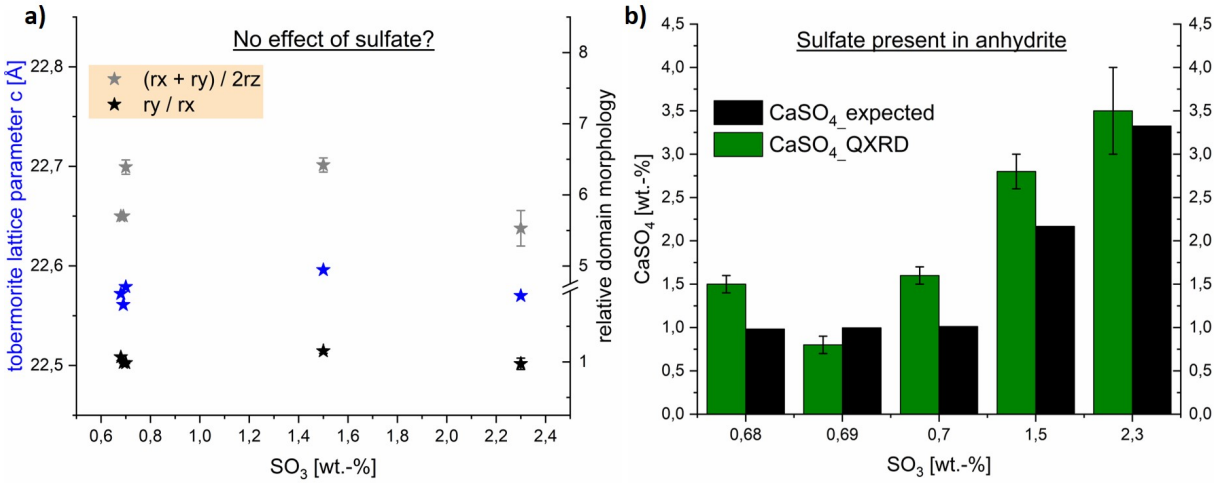

Figure 3.7: Impact of the sulfate content in the AAC raw mix on lattice parameter c and relative domain morphology of tobermorite (a) and comparison of the expected maximum amount of anhydrite to the measured amount determined by QXRD (b).

3.3 Improved monitoring of the phase development during the production of AAC

In this study not only autoclaved samples were analyzed but additionally a lab-scale slurry, which included the reactive components of the green cake stage during AAC production at equivalent weight proportions. In-situ XRD was performed at 70 °C and at a water-to-

solid ratio of 0.8 for 24 h (Figure 3.8), which are respective conditions during commercial production. Clearly, the phase development is dominated by OPC and lime hydration, as described in section 2.2. It can be seen that the major reaction turnover occurs during the first 200 minutes, which is the average duration of the green stage. After only 30 minutes all of the quicklime had transformed into portlandite, whereas Schober proposed a duration of one hour for this reaction [42]. The amount of portlandite is composed of two different generations, as proposed by Ectors [52]. Equally, a biaxial cylinder model was applied in order to fit the peak broadening of the first generation of portlandite in the present investigation. Minor phase developments such as the formation of AFm phases are not shown in Figure 3.8. A coarse fraction of anhydrite did not react, so that constantly around 1.5 wt.% were measured after 6 h. As the decomposition of ettringite due to sulfate depletion [55] does not occur prior to 12 h, the green cake strength is not affected.

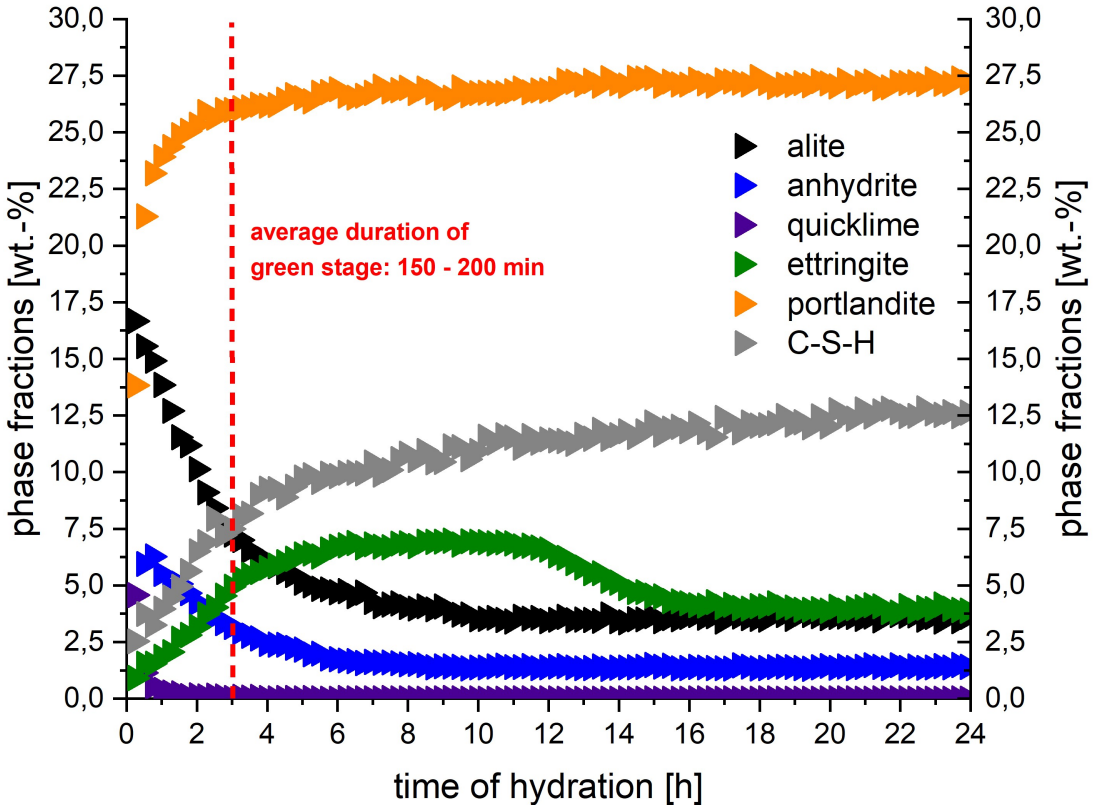

Figure 3.8: In-situ XRD measurement of AAC model slurry at water-to-solid ratio of 0.8 and 70 °C. For clarity and comprehensibility not all phases are shown.

The separation of two generations of portlandite in the system does not only translate into different domain morphologies, as shown by Ectors [52]. In Figure 3.9 more indications for different mineralogical properties are displayed. The shape of the (0 0 1) reflection in XRD patterns after only quicklime hydration and after both, quicklime and alite hydration shows a distinct feature. While portlandite originating from quicklime hydration shows a broad peak implying lower crystallinity, the peak after alite hydration is characterized

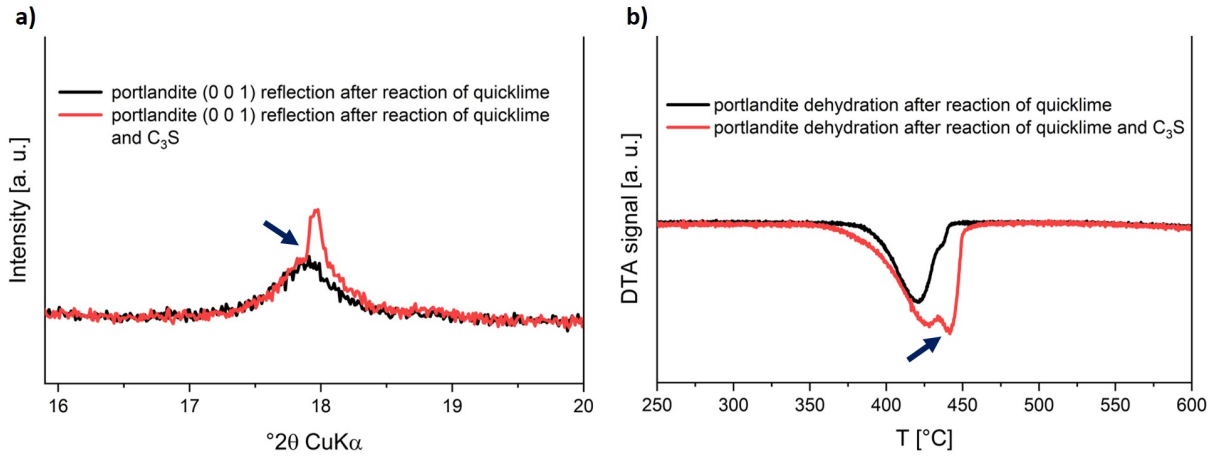

Figure 3.9: Formation of two generations of portlandite in AAC slurry in XRD (a) and DTA (b) plots.

by a sharper component. Yet, the peak breadth did not change, indicating that the first generation is still present with the original characteristics. This observation is supported by DTA measurements, additionally demonstrating two degrees of crystallinity only after alite hydration. In agreement with XRD analysis, the better crystalline second generation of portlandite decomposes at a higher temperature.

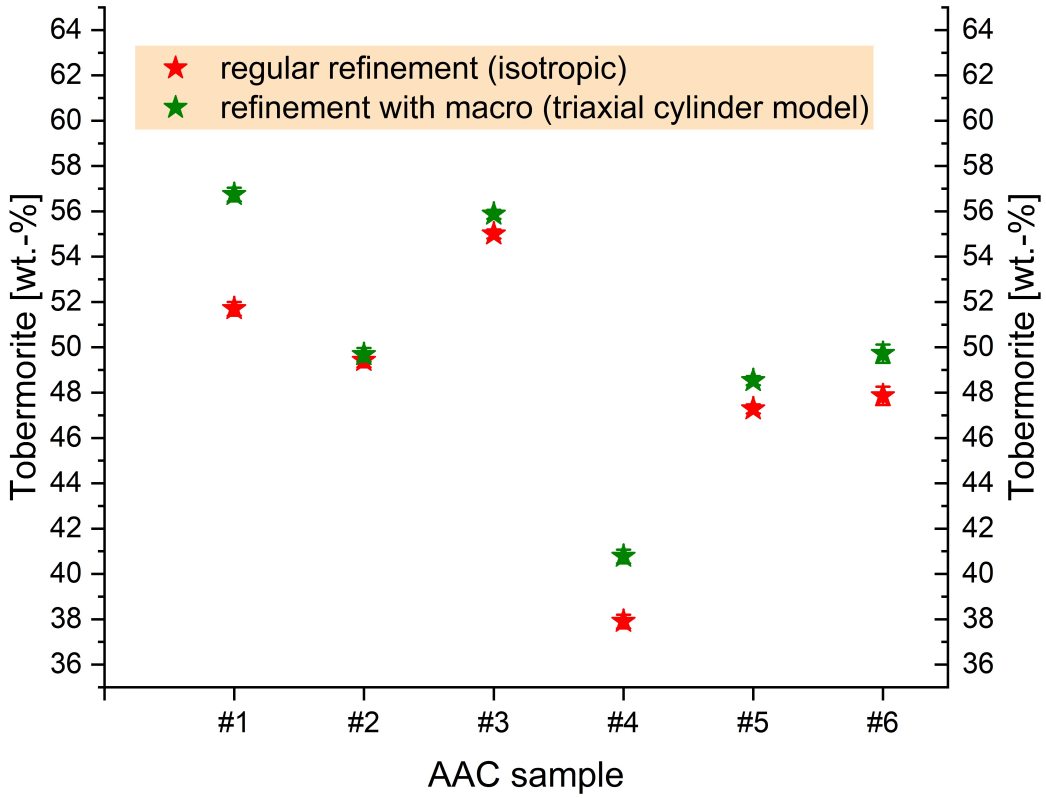

Figure 3.10: Quantification of tobermorite in statistical, chemically various AAC samples with and without the application of the macro for the fitting of anisotropic peak broadening.

Furthermore, commercial AAC samples were considered in this study. By applying the method for the refinement of anisotropic peak broadening (Figure 3.1), a more accurate quantification of tobermorite can be achieved. In Figure 3.10 the calculated amounts of tobermorite in statistical, chemically various AAC samples are plotted. In some samples the refinement using the macro leads to considerably higher but never lower quantities of tobermorite, whereas in other samples nearly the same amount of tobermorite is calculated. This observation can be well understood taking into account that the macro allows to account more peak area for tobermorite, as shown in Figure 3.1. Clearly, there is evidence that the anisotropy of tobermorite domains is not uniform from one sample to another, which was basically justified in the previous sections. As an improved quantification of a single phase leads to a better quantification of other phases in the sample, this adaption is very valuable in order to assess the phase development. Here, the peak broadening of tobermorite equally observed by Qu et al. [6] could be tracked and evaluated in order to gain more accurate results. Moreover, in section 6.3 McCrone milling is suggested in order to avoid spottiness in XRD patterns caused by coarse grains of quartz or anhydrite (Figure 3.8).

4 Conclusions

The research results presented in the previous sections yield advances in the mineralogical investigation of tobermorite and autoclaved aerated concrete. Recorded diffraction patterns contain plenty of usually unused data regarding the microstructural characteristics of the sample and phases therein. The profit of XRD measurements can be significantly improved, whenever one or more phases show anisotropic peak broadening and appropriate models for the respective domain morphology are implemented into the Rietveld environment. Within the scope of the present investigations portlandite and tobermorite show this particularity.

The effects of changes in the chemistry of the starting mix were examined based on different dosages of metakaolin. Al-substituted tobermorite showed increased growth in b direction and an increase of lattice parameter c compared to Al-free tobermorite. The relative domain sizes were determined based on anisotropic peak broadening. However, while the effect of Al^{3+} incorporation into the lattice of tobermorite was limited regarding the domain morphology, lattice parameter c showed an increase throughout the entire range of samples. The consequent effects suggested by Klimesch & Ray observed by means of DTA are debatable, as reactions during the heating experiment may lead to to a change of Al^{3+} content in tobermorite [40]. While both types of applied metakaolin showed good reactivity at hydrothermal conditions, some included minor phases such as feldspar or anatase remained unreacted. At high dosages of Al_2O_3 in the starting mix the formation of either only katoite or katoite along with tobermorite was observed (Figure 3.2).

SEM analysis of tobermorite in AAC cannot be suggested based on the observations presented in this work, as it is only visually accessible in the pores or at pore surfaces. The dense material of the AAC skeleton contains several crystalline and X-ray amorphous phases, which hardly allows a proper investigation. Even in single pores tobermorite crystals appeared very heterogeneous at various chemical compositions. As a result, lath-like tobermorite was not only present in samples characterized by elevated Al^{3+} incorporation. By contrast, the benefits of XRD analysis presented in section 6.1 equally accounted for tobermorite in AAC samples. Sulfate incorporation into the lattice of tobermorite was not observed. All of the sulfate in the system was detected to be present in anhydrite.

The phase transitions in the AAC raw slurry during the green stage hydration were showcased by in-situ XRD analysis of a model mix at 70 °C. Additional DTA and XRD mea-

surements during this step confirmed the presence of two generations of portlandite characterized by different crystallinity as suggested by Ectors [52]. The inclusion of anisotropic domain morphology during the Rietveld refinement allowed a more accurate quantification of tobermorite in autoclaved samples. Sample preparation adjusted to the grain size distribution in AAC samples (section 6.3), the external standard method for quantitative XRD analysis [55] and the approach to evaluate anisotropic peak broadening [19] are the key methods for a more accurate tracking of the phase development during AAC production.

5 References

[1] A. E. Zadov, A. I. Grabezhev, N. N. Pertsev, N. V. Chukanov, and S. V. Pribavkin. Tobermorite-plombierite metasomatites of the Gumeshevsk skarn-porphyry copper deposit, middle Urals. *Doklady Earth Sciences*, 407(3):495–497, 2006.

[2] M. F. Heddle. Preliminary notice of substances which may prove to be new minerals. *Min. Mag.*, 4:117–123, 1880.

[3] S. Merlino, E. Bonaccorsi, and T. Armbruster. The real structure of tobermorite 11Å: Normal and anomalous forms, OD character and polytypic modifications. *European Journal of Mineralogy*, 13(3):577–590, 2001.

[4] C. Biagioni, S. Merlino, and E. Bonaccorsi. The tobermorite supergroup: a new nomenclature. *Mineralogical Magazine*, 79(2):485–495, 2015.

[5] C. A. Ríos, C. D. Williams, and M. A. Fullen. Hydrothermal synthesis of hydrogarnet and tobermorite at 175 °C from kaolinite and metakaolinite in the CaO-Al2O3-SiO2-H2O system: A comparative study. *Applied Clay Science*, 43(2):228–237, 2009.

[6] X. Qu, Z. Zhao, and X. Zhao. Microstructure and characterization of aluminum-incorporated calcium silicate hydrates (C-S-H) under hydrothermal conditions. *RSC Advances*, 8(49):28198–28208, 2018.

[7] R. Šiaučiūnas and K. Baltakys. Formation of gyrolite during hydrothermal synthesis in the mixtures of CaO and amorphous SiO2 or quartz. *Cement and Concrete Research*, 34(11):2029–2036, 2004.

[8] E. Venhodová, R. Janovský, and R. Drochytka. Formation of Tobermorite at Different Materials Composition of Aerated Concrete. *Applied Mechanics and Materials*, 752-753:247–250, 2015.

[9] L. Galvánková, E. Bartoníčková, T. Opravil, J. Tkacz, and P. Ptáček. The influence of starting materials solubility on tobermorite structure formation under the hydrothermal conditions. *IOP Conference Series: Materials Science and Engineering*, 379(1):1–8, 2018.

[10] T. Mitsuda, K. Sasaki, and H. Ishida. Phase Evolution during Autoclaving Process. *J. Am. Ceram. Soc.*, 75(75):1858–1863, 1992.

[11] A. Skawińska. The influence of metahalloysite addition on tobermorite formation studied by X-ray powder diffraction and scanning electron microscope. *MATEC Web of Conferences*, 163:05008, 2018.

[12] S. T. Bergold, F. Goetz-Neunhoeffer, and J. Neubauer. Quantitative analysis of C-S-H in

hydrating alite pastes by in-situ XRD. *Cement and Concrete Research*, 53:119–126, 2013.

[13] O. P. Shrivastava and F. P. Glasser. Ion-exchange properties of 11-Å tobermorite. *Reactivity of Solids*, 2(3):261–268, 1986.

[14] H. Maeda, Y. Ogawa, E. H. Ishida, and T. Kasuga. Hydrothermal synthesis of tobermorite doped with phosphorus species for removing heavy metal ions. *Journal of the Australian Ceramic Society*, 48(1):8–11, 2012.

[15] O. P. Shrivastava and R. Shrivastava. Cation exchange applications of synthetic tobermorite for the immobilization and solidification of cesium and strontium in cement matrix. *Bulletin of Materials Science*, 23(6):515–520, 2000.

[16] G. Renman and A. Renman. Sustainable Use of Crushed Autoclaved Aerated Concrete (CAAC) as a Filter Medium in Wastewater Purification. *8th International conference on sustainable management of waste and recycled materials in construction, Gothenburg, Sweden, 30 May–1 June, 2012. Proceedings*, pages 1–7, 2012.

[17] G. Schober. Chemical transformations during the manufacturing of autoclaved aerated concrete (ACC): Cement, lime, gypsum and quartz sand become cellular concrete. *ZKG*, 58(7):63–70, 2005.

[18] A. J. Hamad. Materials, Production, Properties and Application of Aerated Lightweight Concrete: Review. *International Journal of Materials Science and Engineering*, 2(2):152–157, 2014.

[19] D. Ectors, F. Goetz-Neunhoeffer, and J. Neubauer. A generalized geometric approach to anisotropic peak broadening due to domain morphology. *Journal of Applied Crystallography*, 48(1):189–194, 2015.

[20] H. M. Rietveld. A profile refinement method for nuclear and magnetic structures. *Journal of Applied Crystallography*, 2(2):65–71, 1969.

[21] S. A. Hamid. The crystal structure of the 11 Å natural tobermorite Ca2.25[Si3O7.5(OH)1.5]1H2O. *Zeitschrift fuer Kristallographie - New Crystal Structures*, 154(3-4):189–198, 1981.

[22] S. A. S. El-Hemaly, T. Mitsuda, and H. F. W. Taylor. Synthesis of normal and anomalous tobermorites. *Cement and Concrete Research*, 7:429–438, 1977.

[23] M. Sakiyama and T. Mitsuda. Hydrothermal reaction between C-S-H and kaolinite for the formation of tobermorite at 180°C. *Cement and Concrete Research*, 7(6):681–685, 1977.

[24] E. Bonaccorsi, S. Merlino, and A. R. Kampf. The crystal structure of tobermorite 14 Å (plombierite), a C-S-H phase. *Journal of the American Ceramic Society*, 88(3):505–512, 2005.

[25] S. Merlino, E. Bonaccorsi, and T. Armbruster. The real structures of clinotobermorite and tobermorite 9 Å: OD character, polytypes, and structural relationships. *European Journal of Mineralogy*, 12(2):411–429, 2000.

[26] K. Momma and F. Izumi. VESTA 3 for three-dimensional visualization of crystal, volumetric and morphology data. *Journal of Applied Crystallography*, 44(6):1272–1276, 2011.

[27] S. Shaw, S. M. Clark, and C. M.B. Henderson. Hydrothermal formation of the calcium silicate hydrates, tobermorite (Ca5Si6O16(OH)2 · 4H2O) and xonotlite (Ca6Si6O17(OH)2): An in situ synchrotron study. *Chemical Geology*, 167(1-2):129–140, 2000.

[28] K. Matsui, J. Kikuma, M. Tsunashima, T. Ishikawa, S. Matsuno, A. Ogawa, and M. Sato. In situ time-resolved X-ray diffraction of tobermorite synthesis process under hydrothermal condition. *IOP Conference Series: Materials Science and Engineering*, 18(2):60–66, 2011.

[29] G. Matekonis, R. Šiaučiūnas, and D. Vaičiukynienė. Hydrothermal Synthesis and Characterization of Na + and [Al 3 + + Na +] -substituted Tobermorite in CaO-SiO2 · nH2O-H2O System. *MATERIALS SCIENCE*, 16(3):242–248, 2010.

[30] G. Geng, R. J. Myers, M. J. A. Qomi, and P. J.M. Monteiro. Densification of the interlayer spacing governs the nanomechanical properties of calcium-silicate-hydrate. *Scientific Reports*, 7(1):1–8, 2017.

[31] D. Klimesch and A. Ray. Autoclaved cement-quartz pastes with metakaolin additions. *Advanced Cement Based Materials*, 7(3-4):109–118, 1998.

[32] N. Y. Mostafa, A. A. Shaltout, H. Omar, and S. A. Abo-El-Enein. Hydrothermal synthesis and characterization of aluminium and sulfate substituted 1.1 nm tobermorites. *Journal of Alloys and Compounds*, 467(1-2):332–337, 2009.

[33] İ. Demir, M. S. Başpınar, E. Kahraman, E. Çalışkan, and G. Görhan. An Investigation on the Usability of Diatomite in Aerated Concrete Production. In *Proc. of the Intl. Conf. on Advances In Civil, Structural And Construction Engineering - CSCE 2014*, pages 97–100, 2014.

[34] A. Skawinska, Z. Owsiak, T. Baran, and K. Hernik. The influence of halloysite addition on tobermorite formation in CaO and quartz mix under hydrothermal conditions. *Cement Wapno Beton*, 17(12):426–434, 2017.

[35] N. Y. Mostafa. Influence of air-cooled slag on physicochemical properties of autoclaved aerated concrete. *Cement and Concrete Research*, 35(7):1349–1357, 2005.

[36] D. Małaszkiewicz and J. Chojnowski. Influence of addition of calcium sulfate dihydrate on drying of autoclaved aerated concrete. *Open Engineering*, 7(1):273–278, 2017.

[37] N. Hara and N. Inoue. Thermal behaviour of 11Å tobermorite and its lattice parameters. *Cement and Concrete Research*, (10):53–60, 1980.

[38] M. D. Jackson, S. R. Chae, S. R. Mulcahy, C. Meral, R. Taylor, P. Li, A. H. Emwas, J. Moon, S. Yoon, G. Vola, H. R. Wenk, and P. J.M. Monteiro. Unlocking the secrets of Al-tobermorite in Roman seawater concrete. *American Mineralogist*, 98(10):1669–1687, 2012.

[39] W. Liao, W. Li, Z. Fang, C. Lu, and Z. Xu. Effect of different aluminum substitution rates on the structure of Tobermorite. *Materials*, 12(22):1–10, 2019.

[40] D. Klimesch and A. Ray. DTA-TG Study of the CaO-SiO2-H2O and CaO-Al2O3-SiO2-H2O Systems Under Hydrothermal Conditions. *Journal of Thermal Analysis and Calorimetry*, 56(1):27–34, 1999.

[41] Z. Sauman and Z. Valtr. Substitution of sulphate ions in the crystal lattice of 11 Å tobermorite. In *The VI International Congress on the Chemistry of Cement*, pages 1–14, Moscow, 1974.

[42] G. Schober. Reaction of raw materials to the final product AAC. `http://www.pb-aac.de/chemmin2_e.html`, 2012. accessed 2020-01-31.

[43] D. Jansen, C. Stabler, F. Goetz-Neunhoeffer, S. Dittrich, and J. Neubauer. Does Ordinary Portland Cement contain amorphous phase? A quantitative study using an external standard method. *Powder Diffraction*, 26(01):31–38, 2011.

[44] C. Rößler, J. Stark, F. Steiniger, and W. Tichelaar. Limited-dose electron microscopy reveals the crystallinity of fibrous C-S-H phases. *Journal of the American Ceramic Society*, 89(2):627–632, 2006.

[45] Y. Sakalli and R. Trettin. Investigation of C3S hydration by environmental scanning electron microscope. *Journal of Microscopy*, 259(1):53–58, 2015.

[46] F. Matsushita, Y. Aono, and S. Shibata. Expansion and shrinkage behavior of green cake of Autoclaved Aerated Concrete. In *Autoclaved Aerated Concrete - Innovation and Development: Proceedings of the 4th International Conference on Autoclaved Aerated Concrete, Kingston, UK, 8-9 September 2005*, pages 101–108. CRC Press, 2005.

[47] C. Chucholowski, M. Holger, and K.-C. Thienel. Improving the recyclability, environmental compatibility, and CO2 balance of autoclaved aerated concrete by replacing sulfate carrier and cement with calcined clays. *Ce/Papers*, 2(4):503–512, 2018.

[48] X. Y. Huang, W. Ni, W. H. Cui, Z. J. Wang, and L. P. Zhu. Preparation of autoclaved aerated concrete using copper tailings and blast furnace slag. *Construction and Building Materials*, 27(1):1–5, 2012.

[49] W. Wongkeo and A. Chaipanich. Compressive strength, microstructure and thermal analysis of autoclaved and air cured structural lightweight concrete made with coal bottom ash and silica fume. *Materials Science and Engineering A*, 527(16-17):3676–3684, 2010.

[50] A. Różycka and W. Pichór. Effect of perlite waste addition on the properties of autoclaved aerated concrete. *Construction and Building Materials*, 120:65–71, 2016.

[51] N. Isu, H. Ishida, and T. Mitsuda. Influence of quartz particle size on the chemical and mechanical properties of autoclaved aerated concrete (I) tobermorite formation. *Cement and Concrete Research*, 25(25):243–248, 1995.

[52] D. Ectors. *Advances in the analysis of cementitious reactions and hydrate phases, doctoral thesis*. PhD thesis, Friedrich-Alexander-Universität Erlangen-Nürnberg, 2016.

[53] D. Ectors, F. Goetz-Neunhoeffer, and J. Neubauer. Domain size anisotropy in the double-Voigt approach: An extended model. *Journal of Applied Crystallography*, 48:1998–2001, 2015.

[54] D. Ectors, F. Goetz-Neunhoeffer, and J. Neubauer. Routine (an)isotropic crystallite size analysis in the double-Voigt approximation done right? *Powder Diffraction*, 32(S1):27–34, 2017.

[55] D. Jansen, F. Goetz-Neunhoeffer, C. Stabler, and J. Neubauer. A remastered external standard method applied to the quantification of early OPC hydration. *Cement and Concrete Research*, 41(6):602–608, 2011.

[56] T. Ungár, G. Tichy, J. Gubicza, and R. J. Hellmig. Correlation between subgrains and coherently scattering domains. *Powder Diffraction*, 20(04):366–375, 2005.

[57] Triloki, P. Garg, R. Rai, and B. K. Singh. Structural characterization of as-deposited cesium iodide films studied by X-ray diffraction and transmission electron microscopy techniques. *Nuclear Instruments and Methods in Physics Research, Section A: Accelerators, Spectrometers, Detectors and Associated Equipment*, 736:128–134, 2014.

[58] J. Schreiner, F. Goetz-Neunhoeffer, J. Neubauer, and D. Jansen. Hydrothermal synthesis of 11 Å tobermorite – Effect of adding metakaolin to the basic compound. *Applied Clay Science*, 185, 2020.

[59] J. Schreiner, F. Goetz-Neunhoeffer, J. Neubauer, S. Volkmann, S. Bergold, R. Webler, and D. Jansen. Advanced Rietveld refinement and SEM analysis of tobermorite in chemically diverse autoclaved aerated concrete. *Powder Diffraction*, 34:143–150, 2019.

[60] J. Schreiner, D. Jansen, D. Ectors, F. Goetz-Neunhoeffer, J. Neubauer, and S. Volkmann. New analytical possibilities for monitoring the phase development during the production of autoclaved aerated concrete. *Cement and Concrete Research*, 107:247–252, 2018.

6 Publications

6.1 Hydrothermal synthesis of 11 Å tobermorite – Effect of adding metakaolin to the basic compound

Reprint of the peer reviewed publication

Schreiner, J., Goetz-Neunhoeffer, F., Neubauer, J., Jansen, D., 2020. Hydrothermal synthesis of 11 Å tobermorite – Effect of adding metakaolin to the basic compound. Applied Clay Science **185**, https://doi.org/10.1016/j.clay.2019.105432

Applied Clay Science 185 (2020) 105432

Contents lists available at ScienceDirect

Applied Clay Science

journal homepage: www.elsevier.com/locate/clay

Research paper

Hydrothermal synthesis of 11 Å tobermorite – Effect of adding metakaolin to the basic compound

J. Schreiner*, F. Goetz-Neunhoeffer, J. Neubauer, D. Jansen

University of Erlangen-Nuremberg, GeoZentrum Nordbayern, Mineralogy, Schlossgarten 5a, 91054 Erlangen, Germany

ARTICLE INFO

Keywords:
Hydrothermal synthesis
11 Å tobermorite
Metakaolin
Powder diffraction
Katoite

ABSTRACT

Different amounts and types of metakaolin were analyzed and applied for the hydrothermal synthesis of 11 Å tobermorite. All synthesized samples were investigated by means of powder XRD combined with Rietveld refinement. Al-substituted 11 Å tobermorite was successfully synthesized on the basis of a broad range of compounds characterized by a varying content of metakaolin. Katoite was present depending on the amount of supplied Al^{3+}, which was determined by the dosage of metakaolin. Minor crystalline components included in the two types of metakaolin sources varied greatly in their reactivity under hydrothermal conditions. Despite a different degree of purity, the two types of metakaolin showed corresponding effects at moderate dosages but contrary effects at higher dosages as for the synthesis of 11 Å tobermorite. The domain morphology of tobermorite could be associated with Al^{3+} incorporation for low dosages of metakaolin represented by up to 2 wt.-% Al_2O_3 in the dry mix. By contrast, Al^{3+} affected tobermorite lattice parameters at equivalent and even at higher dosages with *c* reaching 22.95 Å at 12 wt.-% Al_2O_3 in the dry mix.

1. Introduction

1.1. Application of metakaolin as a reactive material in construction industry

The application of supplementary cementitious materials (SCMs) in the field of construction technology has received a lot of attention in recent years. Due to limited resources and an urgent need for alternative and more eco-friendly construction materials, SCMs such as metakaolin offer a great potential. The usage of SCMs has not only spread to the cement and mortar industry but also to advanced applications such as autoclaved aerated concrete (AAC) (Demir et al., 2014; Koutný et al., 2014; Walczak et al., 2015; Różycka and Pichór, 2016; Chucholowski et al., 2018). Unlike ordinary cementitious construction materials, AAC is produced from hydrothermal curing. Due to the different thermodynamic environment, the hydration process and the reactivity of raw materials have to be investigated properly in order to understand the effects on the AAC product. The leading mineral phase in AAC is 11 Å tobermorite ($Ca_5Si_6O_{16}(OH)_2{\cdot}4H_2O$). As a consequence, the thermal and mechanical properties of AAC depend on microstructure and crystallinity of tobermorite to some extent. In addition to the curing time and the fineness of raw materials, the supply of ions that can substitute in the tobermorite structure is a crucial factor in this context. Especially substitutions by aluminum, sodium and potassium ions have been investigated thoroughly (Sauman, 1974; Klimesch and Ray, 1998; Mostafa et al., 2009; Matekonis et al., 2010; Skawinska et al., 2017). Calcined clays usually contain a considerable amount of the mentioned ions.

There is a vast amount of literature on the reactivity of SCMs at ambient temperature and standard pressure, but there is little when it comes to hydrothermal conditions. In previous publications the behavior of metakaolin under hydrothermal conditions was mainly investigated for the synthesis of zeolites (Zhang et al., 2007; Aguilar-Mamani et al., 2014; Setthaya et al., 2016; Luo et al., 2018). In these studies, the reactivity of metakaolin was observed at a wide range of temperature and pH values. During the transformation of kaolin into metakaolin, a loss of framework alumina was observed (Ayodele et al., 2019). In recent decades, metakaolin has been the subject of studies in the field of geopolymer research (Rashad, 2013; Chen et al., 2016). For the synthesis of 11 Å tobermorite a more distinct setting of temperature setting (180–200 °C) and steam pressure (1–1.2 MPa) are required.

This publication is intended to make a new contribution to the challenging field of hydrothermal synthesis in the system CaO-Al_2O_3-SiO_2-H_2O based on XRD analysis combined with Rietveld refinement. Various dosages of two types of metakaolin with different chemical and mineralogical purities are compared for the effects on the hydrothermal synthesis of Al-substituted 11 Å tobermorite. Especially changes of the bulk chemistry in the raw mixes, the reactivity of minor crystalline

* Corresponding author.
E-mail address: juergen.js.schreiner@fau.de (J. Schreiner).

https://doi.org/10.1016/j.clay.2019.105432
Received 20 August 2019; Received in revised form 13 November 2019; Accepted 30 December 2019

phases of the two types of metakaolin and the effect of different curing times are the focus of interest. On the one hand, metakaolin offers a great potential in the AAC industry. On the other hand, of all SCMs, metakaolin is a good source material for investigating the influence of Al^{3+} on the synthesis of Al-substituted 11 Å tobermorite.

1.2. Synthesis of Al-substituted 11 Å tobermorite

In addition to being present in AAC, tobermorite has found application in wastewater treatment and nuclear waste management due to its ion exchange capacity (Maeda et al., 2012; Monasterio et al., 2015). The substitution of silicon by aluminum results in a different tobermorite structure due to general and local charge balance affecting the lattice parameters. Especially *c* is impacted by this substitution because it occurs in the bridging tetrahedron and additional OH^- substitutes O^{2-} (Komarneni et al., 1985; Merlino et al., 2000). As suggested in some additional studies, the substitution of Si^{4+} by Al^{3+} and Na^+ or K^+ leads to a lath-like morphology of tobermorite crystals (Mostafa, 2005; Mostafa et al., 2009; Venhodová et al., 2015; Qu et al., 2018). However, because of the heterogeneous appearance of tobermorite in AAC it is hardly possible to conduct a proper characterization based on SEM analysis. In our recent work, the anisotropic peak broadening of tobermorite in XRD diffractograms was successfully linked with the incorporation of foreign ions supplied in a common AAC production (Schreiner et al., 2019). This finding allowed a more statistical structural characterization of tobermorite in bulk compositions compared to SEM analysis. Moreover, it was reported in other studies, that different hydrate phases occur depending on the amount of supplied ions and on the experimental settings. In compounds with a high content of Al^{3+}, formation of katoite could be observed (Klimesch and Ray, 1998; Ríos et al., 2009; Matsui et al., 2011). In the case of a longer curing duration, instead of 11 Å tobermorite the formation of xonotlite (Siauciunas and Baltakys, 2004; Galvánková et al., 2018) or - depending on the fineness of used silica source (Siauciunas and Baltakys, 2004) - gyrolite is favoured.

Kalousek (1956) suggested that tobermorite can contain up to 5% Al_2O_3. More Al_2O_3 in the system resulted in the formation of hydrogarnet. Klimesch and Ray (1998) additionally investigated the stability of hydrogarnet depending on the Al/(Si + Al) ratio and its role in relation to the formation of 11 Å tobermorite in an equivalent system. They suggest that hydrogarnet always appears before tobermorite but the former can only be detected for higher Al/(Si + Al) ratios in the event of longer curing times. Ríos et al. (2009) and Qu et al. (2018) confirmed these findings in extensive investigations. In the latter publication it is additionally suggested that samples prepared at lower temperatures (160 °C) are less impacted by the supply of Al^{3+}. They also consider the peak broadening of tobermorite in their XRD plots based on the amount of incorporated Al^{3+}. In two recent publications we suggested that the peak broadening of tobermorite enables a microstructural analysis by calculating the orientation dependent domain sizes (Schreiner et al., 2018, 2019). However, these studies are based on samples of industrially produced AAC, so that the curing time was fixed. The studied AAC was produced from raw materials with a broad chemical spectrum such as ordinary Portland cement (OPC), which somehow complicates the interpretation of results.

In this work the influence of aluminum ions - provided by metakaolin - on dominant crystallographic direction-dependent domain growth of tobermorite is investigated by analysis of anisotropic peak broadening (Ectors et al., 2015, 2017). In Fig. 1 of the supplementary material, the method of fitting the anisotropic peak broadening of tobermorite using a triaxial cylinder model is visualized (Schreiner et al., 2018) Fitting of the anisotropic peak broadening of tobermorite. This method is used to calculate the average and reliable values for tobermorite domain sizes in the powder sample and associate them with average Al^{3+} incorporation. Microstrain should be considered because it is an additional source of peak broadening. However, this usually accounts for materials, that have been exposed to different kinds of stress such as metals and alloys (Badawi et al., 2019). In addition, the instrumental contribution to peak broadening should be considered. Hydration products such as tobermorite are characterized by crystallite sizes in the range of nanometers, so that anisotropic size broadening clearly outweighs the effect of instrumental broadening (Jenkins and Snyder, 1996). Moreover, the impact of Al^{3+} on the lattice parameters of tobermorite is considered. It should additionally be clarified, whether the results from our previous publication (Schreiner et al., 2019) based on industrially produced AAC can be confirmed by investigation with less complex raw mixes and purely based on laboratory experiments.

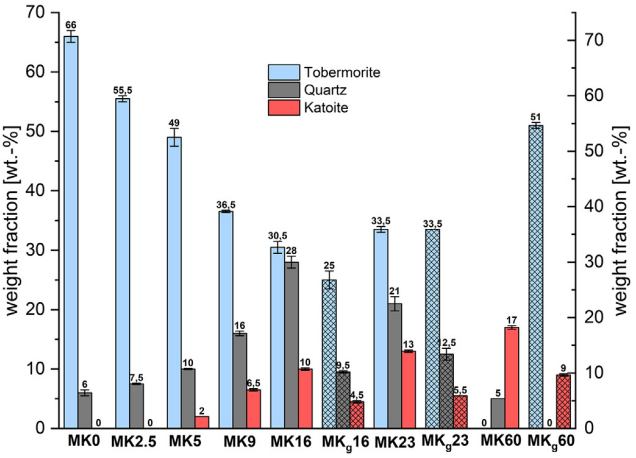

Fig. 1. Weight fractions of tobermorite, quartz and katoite determined by quantitative XRD analysis – samples including MK_g crosshatched.

2. Material and methods

2.1. Starting materials

The starting materials for hydrothermal synthesis included deionized water, quartz flour, portlandite (99.9% pure) and two types of metakaolin. One type was ordinary, commercially available metakaolin (MK) with nearly a stoichiometric composition. For comparison, the second type of commercially available metakaolin was a by-product from expanded glass production (MK_g) and consequently highly impure. The chemical composition of MK and MK_g determined by XRF is given in Table 1. With MK_g containing less Al_2O_3 but considerably more Na_2O than MK, the effects on hydrothermal synthesis were of interest. Both types of metakaolin have been characterized in previous publications (Schmidt et al., 2012; Naber et al., 2019). In addition, we verified the mineral phase content by XRD analysis. Besides amorphous metakaolin, MK contained minor amounts of anatase, quartz and mica.

Table 1
Chemical composition of MK and MK_g determined by XRF analysis – major contrasts in bold letters.

Oxides [wt.-%]	MK	MK_g
SiO_2	53.6	60.4
Al_2O_3	**39.2**	**20.6**
CaO	0.1	4.0
MgO	0.1	1.2
Na_2O	**0**	**9.6**
K_2O	1.0	1.8
Fe_2O_3	1.8	0.5
TiO_2	2.1	0.3
P_2O_5	0.1	0.2
Loss on ignition	1.5	1

Table 2
Basic powder compounds prepared for the hydrothermal synthesis of tobermorite with the respectively calculated Al_2O_3 content and curing time in the reactor.

Sample	Portlandite [wt.-%]	Quartz [wt.-%]	MK [wt.-%]	MK_g [wt.-%]	Al_2O_3 [wt.-%]	Curing time [h]
MK0	49	51	–	–	0	12
MK2.5	49.5	48	2.5	–	1	12
MK5	49	46	5	–	2	12
MK9_2h	48	43	9	–	3.5	2
MK9_6h	48	43	9	–	3.5	6
MK9_12h	48	43	9	–	3.5	12
MK16	47	37	16	–	6.3	12
MK23	46	31	23	–	9	12
MK60	40	–	60	–	23.5	12
MK_g16	47	37	–	16	3.3	12
MK_g23	46	31	–	23	4.7	12
MK_g60	40	–	–	60	12.4	12

MK_g contained additional kaolinite, feldspar and quartz.

2.2. Investigated mix composites

For the preparation of raw mixtures, the powders were weighed and homogenized using a lab-scale mixing mill. Table 2 lists the composition and nomenclature of all samples including Al_2O_3 content and curing time in the autoclave.

- Besides one blank mixture (MK0) that did not contain any type of metakaolin, eleven more compounds were prepared, of which three included different dosages of MK_g (MK_g16, MK_g23 and MK_g60). Three more mixes contained equivalent amounts of MK instead of MK_g (MK16, MK23 and MK60). These mixes were investigated in order to have a direct comparison concerning the effects of different raw material on the synthesis of tobermorite.
- Additionally the mixes MK9, MK5 and MK2.5 with lower dosages of metakaolin were analyzed. In the referenced literature (Schreiner et al., 2019), the effect of Al^{3+} on the anisotropic peak broadening of tobermorite could only be observed in the case of Al_2O_3 contents lower than 4% in the drymix. In the latter three mixes Al_2O_3 contents range from 1 to 3.5% Al_2O_3 (calculated from XRF data), which meets the region of interest for the analysis of tobermorite domain morphology.
- The curing time for nearly all of the investigated samples was 12 h but compound MK9 was prepared two more times for curing times of 2 h and 6 h. The different curing times were chosen in this particular sample, so that the reactivity of metakaolin and the phase transitions could be observed more precisely.

2.3. Hydrothermal treatment

Due to the different fineness of raw materials, there was a different water demand from one mixture to another. In order to obtain slurries of comparable rheology, the amount of water was adapted respectively resulting in water-to-solid ratios of 2.5 to 3, which matches the suggested water-to-solid ratio for this purpose (Rózycka et al., 2014; Galvánková et al., 2018). The weighed water was added to the dry mix and after stirring for 1 min at 23 °C the slurry was poured into the reactor. Minor changes in the quantity of added water did not have an influence on the measured steam pressure. All experiments were conducted using a PTFE-lined stainless steel autoclave with a reactor volume of 300 ml. The oven temperature was fixed at 180 °C and autogenous steam pressure of 1.1–1.2 MPa was measured during each experiment with an external manometer. After cooling to room temperature, the sample was removed from the reactor, coarsely ground using an agate mortar and dried at 60 °C for 12 h. After drying, the sample was ground with an agate mortar again in order to deagglomerate the particles. As no coarse raw materials were used, there was no need for wet McCrone milling (Schreiner et al., 2018).

Table 3
Structural data used for the investigation with powder XRD analysis.

Phase	Author
Anatase	(Horn et al., 1972)
Biotite	(Brigatti et al., 2000)
Calcite	(Maslen et al., 1995)
Kaolinite	(Zvyagin, 1960)
Katoite	(Bartl, 1969)
Microcline	(Bailey, 1969)
Plazolite	(Basso et al., 1983)
Portlandite	(Busing and Levy, 1957)
Quartz	(Le Page and Donnay, 1976)
Scawtite	(Grice, 2005)
Tobermorite	(Hamid, 1981)
Xonotlite	(Hejny and Armbruster, 2001)

2.4. XRD analysis

After preparation into front-loading sample holders, the powder samples were measured with a D8 diffractometer (Bruker) equipped with a LynxEye detection system and Bragg-Brentano geometry. The settings for XRD analysis included a tube voltage of 40 kV, a current of 40 mA, an angular range from 6 to 80° 2θ (Cu Kα radiation), a time per step of 0.54 s, a step width of 0.0236° 2θ and a PSD opening of 3.3°. The background was fitted with Chebyshev polynomial of the fifth order. The major contribution of amorphous phase was fitted with a single peak with a fixed position at 30.8° 2θ, so that tobermorite reflections were not affected. An external quartzite standard was measured with the same parameters in order to determine phase quantities (Jansen et al., 2011). Bruker AXS software TOPAS 5.0 was used for Rietveld refinement (Rietveld, 1969) and the used structures are shown in Table 3.

3. Results and discussion

3.1. Different dosages of MK and MK_g

In Fig. 1, the quantities of tobermorite, quartz and katoite present in most of the samples determined by XRD analysis are illustrated. Whenever tobermorite was the leading mineral hydrate phase, a basal spacing of 11.3 Å could be verified in each of the diffractograms. The quantities of minor crystalline phases and amorphous content are not shown. For low dosages of MK, it can be seen that the weight fraction of tobermorite decreased. At moderate dosage of both types of metakaolin (MK16, MK23, MK_g16, MK_g23) tobermorite was present in comparable quantities. It can be seen that the amount of katoite in the mixes depended on the dosage of metakaolin, and it appeared only at dosages of MK5 or more. Due to the higher content of aluminum in MK compared to MK_g, more katoite could always be observed in the MK mixes at equivalent dosages. Despite equal amounts of quartz as starting material in mixes for both types of metakaolin, the resulting weight fractions in the cured samples were not alike. Considerably more quartz was present in the MK samples. Even though less quartz was used for mixes containing higher amounts of MK, even more quartz was present after hydrothermal curing (Table 2, Fig. 1). Consequently, some of the SiO_2 provided by MK did not transform into an amorphous phase or tobermorite but into quartz. This finding is verified by the presence of quartz in MK60 because no quartz was included in the raw mixture. The feldspar present in MK_g did not react, so Na_2O and an unknown amount of Al_2O_3 may not have been supplied for hydrothermal reaction. Besides tobermorite and quartz, additional calcite, scawtite ($Ca_7Si_6(CO_3)$

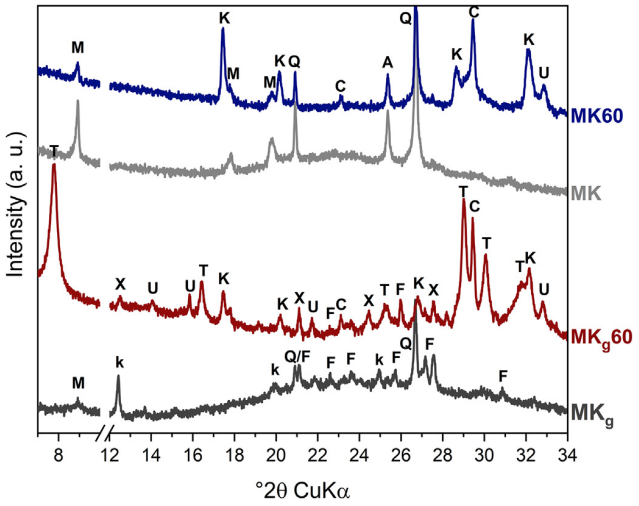

Fig. 2. Diffractograms of MK_g, MK_g60, MK and MK60 from 7 to 34°2θ CuKα. A, anatase; C, calcite; F, feldspar; k, kaolinite; K, katoite; M, mica; Q, quartz; T, tobermorite; U, unidentified phase; X, xonotlite.

O_{18}•2(H_2O)) and xonotlite ($Ca_6Si_6O_{17}(OH)_2$) could be identified in sample MK0 (XRD plots of samples MK0, MKg16, MKg23, MK16 and MK23.). Comparing MK0 and MK2.5, scawtite and xonotlite could still be identified in a very low amount in MK2.5, but no longer in samples that contained even more MK (XRD plots of samples MK0, MK2.5, MK5 and MK9_12h.).

Two additional experiments were done without quartz in the raw mixes (MK60 and MK_g60). The according diffractograms after hydrothermal curing are shown in Fig. 2. In sample MK_g60 tobermorite (> 50 wt.-%) was successfully synthesized without any other silica source than MK_g, whereas no crystalline quartz occurred. By contrast, no tobermorite but quartz could be identified in equivalent mixture MK60 containing MK. It can be seen that crystalline components such as mica and anatase in the raw MK did not react at the selected conditions and remained present in the autoclaved samples. Except for feldspar in MK_g, all of the crystalline components appeared to be reactive at the chosen hydrothermal conditions. A minor unidentified phase occurred at 32.8°2θ and additional xonotlite was identified in sample MK_g60. In sample MK60 more calcium was needed for the formation of more hydrogarnet (Fig. 1) resulting in a lower Ca/Si ratio for the remaining system. Sample MK_g60 contained only half of the amount of Al^{3+} and it was not completely supplied for reaction due to its partial presence in feldspar. Consequently, essentially less hydrogarnet (Fig. 1) was present in MK_g60 after hydrothermal treatment and the Ca/Si ratio in the remaining system was affected to a lesser extent.

3.2. Application of MK for different curing times

The development of hydrate phases in the autoclave for compound MK9 is displayed in Fig. 3. After only 2 h of hydrothermal curing all of the available portlandite had reacted and katoite (9.5 wt.-%) was present. The applied type of metakaolin appeared to react quickly, as it supplied aluminum for formation of katoite. No formation of tobermorite could be observed at this stage yet. An assumably amorphous precursor can be seen at 28 to 30°2θ. Calcium was provided by the dissolution of portlandite. After 6 h of hydrothermal reaction amounts of katoite (8.5 wt.-%) and quartz (from 31 wt.-% at 2 h to 16.5 wt.-% at 6 h) had decreased and a major amount of tobermorite (35 wt.-%) was present. Apparently, between 2 and 6 h under hydrothermal conditions, the amorphous precursor and quartz reacted resulting in the formation of tobermorite. An additional 6 h of reaction time (MK9_12h) did not change the phase composition significantly. Slightly more tobermorite (36.5 wt.-%), less quartz (16 wt.-%) and katoite (6.5 wt.-%) were measured.

3.3. Tobermorite domain morphology and lattice parameters

In the referenced literature, an analysis of tobermorite domain morphology based on anisotropic peak broadening was possible for samples that contained not > 4 wt.-% Al_2O_3 in the drymix (Schreiner et al., 2019). Accordingly, in this study samples MK0, MK2.5, MK5, MK9_6h and MK9_12h were suitable (Table 2) with MK9_2h not containing any tobermorite. In Fig. 4 the respective growth in a and b direction is visualized with x indicating the domain size in *a* direction and y indicating domain size in *b* direction using a macro for TOPAS 5.0 (Ectors et al., 2015, 2017). The calculated cylinder models in Fig. 4 represent the relation of y/x and not absolute sizes. With no supply of aluminum ions (MK0), the relative domain growth in *b* direction is lower compared to samples containing metakaolin. This finding agrees with the results from a similar investigation of tobermorite in AAC (Schreiner et al., 2019). However, within the samples MK5 and MK9_12h the different amounts of supplied aluminum ions did not show a clear effect. It appeared that low dosages of Al^{3+} (1 wt.-% Al_2O_3 in MK2.5 and 2 wt.-% Al_2O_3 in MK5) were enough to determine the domain growth of tobermorite. Additional results from the samples MK9_6h and MK9_12h indicated that growth in b direction increased with reaction time.

In Fig. 5 lattice parameters of tobermorite depending on metakaolin dosages are plotted. *B* clearly remained unaffected throughout the range of samples. Increasing amounts of metakaolin led to a slightly smaller parameter *a*. However, both types of metakaolin showed a corresponding impact on parameter *a*. By contrast, parameter *c* increased strongly with increasing amounts of MK and MK_g, but the type of metakaolin was significant. At an equivalent dosage, MK affected the cell dimension in *c* direction considerably more than MK_g, so that the fraction of Al^{3+} appeared to be the decisive parameter. Different metal oxides in MK_g did not show a notable effect, certainly, as they were partially not provided for reaction. Unlike for the domain morphology of tobermorite, the impact on lattice parameters could be observed within the complete range of examined dosages.

4. Conclusions

The results obtained from the introduced investigations allow concluding remarks on the effects of the applied types of metakaolin on the synthesis of 11 Å tobermorite, the phase transitions and the incorporation of Al^{3+} into the lattice of tobermorite.

With a critical dosage, the use of any type of metakaolin led to the formation of katoite in an according amount. At moderate dosages (MK_g16, MK_g23, MK16 and MK23) the two types of metakaolin showed a good correspondence in consideration of the quantities of tobermorite. For higher dosages, there were contrary effects. Lower dosages of MK led to considerable quantities of Al-substituted tobermorite. Samples containing low dosages of MK revealed that katoite appeared in the case of > 5 wt.-% of MK - corresponding to 2 wt.-% Al_2O_3 - in the basic compound. Minor crystalline phases in MK_g showed better reactivity than those in MK. The observation that no tobermorite was present in sample MK60 indicated that high dosages of Al^{3+} hindered the formation of tobermorite.

Investigations of MK9 at 2, 6 and 12 h displayed the evolution of hydrate phases. At first, katoite was the only crystalline hydrate phase present after 2 h, which corresponded to observations in a different publication (Klimesch and Ray, 1999). The amount of katoite and quartz then decreased and a major amount of tobermorite formed from 2 to 6 h curing time. In order to gain more information on the transformation of amorphous C-(A)-S-H into tobermorite, additional experiments in the range of 2 to 6 h curing time will be needed.

Domain morphology analysis of tobermorite revealed that low

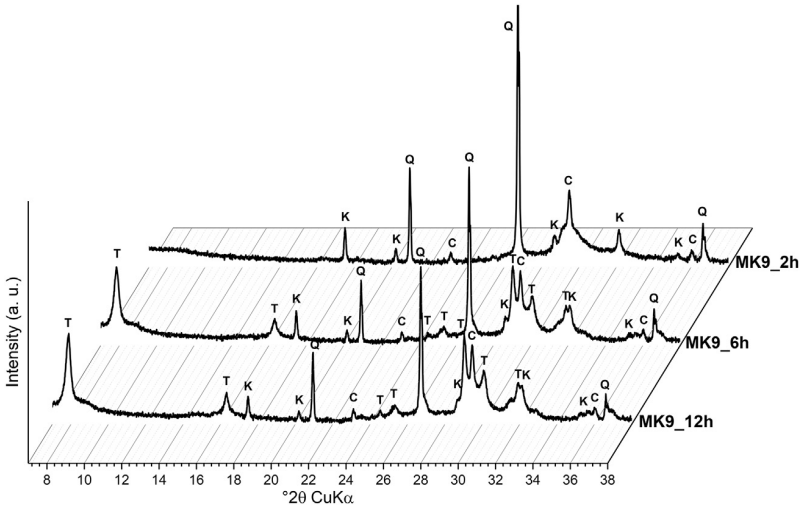

Fig. 3. Diffractograms of MK9_2h, MK9_6h and MK9_12h from 7 to 38°2θ CuKα. C, calcite; K, katoite; Q, quartz; T, tobermorite.

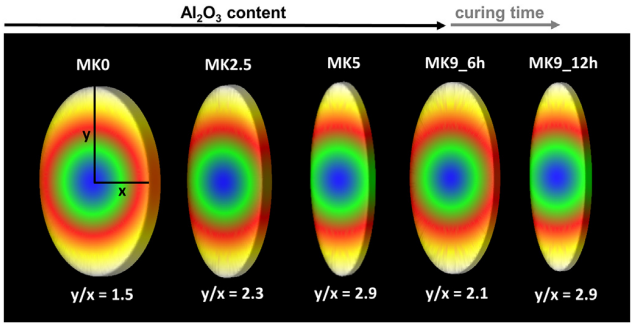

Fig. 4. Relation of calculated domain sizes of 11 Å tobermorite in selected samples (MK0, MK2.5, MK5, MK9_6h and MK9_12h) in a (x) and b (y) direction.

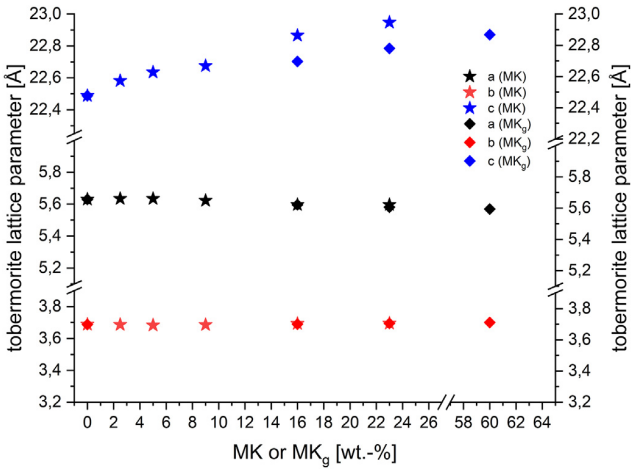

Fig. 5. Lattice parameters of tobermorite depending on MK or MK_g dosage including blank mix MK0.

dosages of Al^{3+} determined the domain growth, which agreed with the results published on tobermorite in AAC samples (Schreiner et al., 2019). Different curing times unveiled that growth in b direction increased with the reaction time. Al^{3+} incorporation into the lattice of tobermorite only reflected to a limited extent in the domain morphology. By contrast, an increase of lattice parameter *c* was triggered by Al^{3+} even at the highest dosage in this study. Ultimately, there is no evidence for a limit of incorporation of Al^{3+} but there is a limit of influence on the domain morphology. These results additionally reconfirm this assumption similarly made in the previous work (Schreiner et al., 2019) and suggest a new mechanism of tobermorite crystallization depending on the presence of Al^{3+}.

Supplementary data to this article can be found online at https://doi.org/10.1016/j.clay.2019.105432.

Declaration of Competing Interest

The authors declare that they have no known competing financial interests or personal relationships that could have appeared to influence the work reported in this paper.

Acknowledgement

The authors thank Rodgauer Baustoffwerke GmbH & Co. KG for supplying raw materials for laboratory experiments.

References

Aguilar-Mamani, W., García, G., Hedlund, J., Mouzon, J., 2014. Comparison between leached metakaolin and leached diatomaceous earth as raw materials for the synthesis of ZSM-5. Springerplus 3, 1–10. https://doi.org/10.1186/2193-1801-3-292.

Ayodele, O.B., Sulaimon, A.A., Alaba, P.A., Tian, Z.-Y., 2019. Influence of metakaolinization temperature on the structure and activity of metakaolin supported Ni catalyst in dry methane reforming. J. Environ. Chem. Eng. https://doi.org/10.1016/j.jece.2019.103239. (in press).

Badawi, E.A., Abdel-Rahman, M.A., Mostafa, A., Abdel-Rahman, M., 2019. Determination of the crystallite size & micro- strain by novel method from XRD profile. Appl. Phys. 2, 1–15. https://doi.org/10.31058/j.ap.2019.21001.

Bailey, S.W., 1969. Refinement of an intermediate microcline structure. Am. Miner. 54, 1540–1545.

Bartl, H., 1969. Roentgen-Einkristalluntersuchungen an (CaO)3 (Al2O3) (H2O)6 und an (CaO)12 (Al2O3)7 (H2O), neuer Vorschlag zur (CaO)12 (Al2O3)7-Struktur. Neues Jahrb. fuer Mineral. Monatshefte 1969, 404–413.

Basso, R., Giusta, A.D., Zefiro, L., 1983. Crystal structure refinement of plazolite. A highly hydrated natural hydrogrossular. Neues Jahrb Miner. Monatsh (Neues Jahrb. fuer Mineral. Monatshefte) 1983, 251–258.

Brigatti, M.F., Lugli, C., Poppi, L., Foord, E.E., Kile, D.E., 2000. Crystal chemical variations in Li- and Fe-rich micas from Pikes Peak batholith (Central Colorado). Am. Mineral. 85, 1275–1286. https://doi.org/10.2138/am-2000-8-920.

Busing, W.R., Levy, H.A., 1957. Neutron diffraction study of calcium hydroxide. J. Chem. Phys. 26, 563. https://doi.org/10.1063/1.1743345.

Chen, L., Wang, Z., Wang, Y., Feng, J., 2016. Preparation and properties of alkali activated metakaolin-based geopolymer. Materials (Basel) 9, 1–12. https://doi.org/10.3390/ma9090767.

Chucholowski, C., Holger, M., Thienel, K.-C., 2018. Improving the recyclability, environmental compatibility, and CO2 balance of autoclaved aerated concrete by replacing sulfate carrier and cement with calcined clays. Ce/Papers 2, 503–512. https://doi.org/10.1002/cepa.846.

Demir, İ., Başpınar, M.S., Kahraman, E., Çalışkan, E., Görhan, G., 2014. An investigation on the usability of diatomite in aerated concrete production. In: Proc. of the Intl. Conf. on Advances in Civil, Structural and Construction Engineering – CSCE 2014, pp. 97–100.

Ectors, D., Goetz-Neunhoeffer, F., Neubauer, J., 2015. A generalized geometric approach to anisotropic peak broadening due to domain morphology. J. Appl. Crystallogr. 48, 189–194. https://doi.org/10.1107/S1600576714026557.

Ectors, D., Goetz-Neunhoeffer, F., Neubauer, J., 2017. Routine (an)isotropic crystallite size analysis in the double-Voigt approximation done right? Powder Diffract. 32, 27–34. https://doi.org/10.1017/S0885715617000070.

Galvánková, L., Bartoníčková, E., Opravil, T., Tkacz, J., Ptáček, P., 2018. The influence of starting materials solubility on tobermorite structure formation under the hydrothermal conditions. IOP Conf. Ser. Mater. Sci. Eng. 379, 1–8. https://doi.org/10.1088/1757-899X/379/1/012001.

Grice, J.D., 2005. The structure of spurrite, tilleyite and scawtite, and relationships to other silicate-carbonate minerals. Can. Mineral. 43, 1489–1500. https://doi.org/10.2113/gscanmin.43.5.1489.

Hamid, S.A., 1981. The crystal structure of the 11 Å natural tobermorite Ca2.25[Si3O7.5(OH)1.5]1H2O. Zeitschrift fuer Krist. 154, 189–198. https://doi.org/10.1524/zkri.1981.154.3-4.189.

Hejny, C., Armbruster, T., 2001. Polytypism in xonotlite Ca6Si6O17(OH)2. Zeitschrift fur Krist. 216, 396–408.

Horn, M., Schwerdtfeger, C.F., Meagher, E.P., 1972. Refinement of the structure of anatase at several temperatures. Zeitschrift fur Krist. 136, 273–281. https://doi.org/10.1524/zkri.1972.136.3-4.273.

Jansen, D., Goetz-Neunhoeffer, F., Stabler, C., Neubauer, J., 2011. A remastered external standard method applied to the quantification of early OPC hydration. Cem. Concr. Res. 41, 602–608. https://doi.org/10.1016/j.cemconres.2011.03.004.

Jenkins, R., Snyder, R., 1996. Introduction to X-ray Powder Diffractometry, Chemical Analysis. Wiley, pp. 90.

Kalousek, G.L., 1956. Crystal Chemistry of Hydrous Calcium Silicates. J. Am. Ceram. Soc. 40, 74–80.

Klimesch, D., Ray, A., 1998. Autoclaved cement-quartz pastes with metakaolin additions. Adv. Cem. Based Mater. 7, 109–118. https://doi.org/10.1016/S1065-7355(97)00073-4.

Klimesch, D., Ray, A., 1999. DTA-TGA evaluations of the CaO–Al2O3–SiO2–H2O system treated hydrothermally. Thermochim. Acta 334, 115–122. https://doi.org/10.1016/s0040-6031(99)00140-9.

Komarneni, S., Roy, R., Roy, D.M., Fyfe, C.A., Kennedy, G.J., Bothner-By, A.A., Dadok, J., Chesnick, A.S., 1985. 27Al and29Si magic angle spinning nuclear magnetic resonance spectroscopy of Al-substituted tobermorites. J. Mater. Sci. 20, 4209–4214. https://doi.org/10.1007/BF00552416.

Koutný, O., Opravil, T., Pořízka, J., 2014. Application of metakaoline in autoclaved aerated concrete technology. Adv. Mater. Res. 1000, 174–177. https://doi.org/10.4028/www.scientific.net/AMR.1000.174.

Le Page, Y., Donnay, G., 1976. Refinement of the crystal structure of low-quartz. Acta Crystallogr. Sect. B 32, 2456–2459. https://doi.org/10.1107/S0567740876007966.

Luo, H., Law, W.W., Wu, Y., Zhu, W., Yang, E.H., 2018. Hydrothermal synthesis of needle-like nanocrystalline zeolites from metakaolin and their applications for efficient removal of organic pollutants and heavy metals. Microporous Mesoporous Mater. 272, 8–15. https://doi.org/10.1016/j.micromeso.2018.06.015.

Maeda, H., Ogawa, Y., Ishida, E.H., Kasuga, T., 2012. Hydrothermal synthesis of tobermorite doped with phosphorus species for removing heavy metal ions. J. Aust. Ceram. Soc. 48, 8–11.

Maslen, E.N., Streltsov, V.A., Streltsova, N.R., Ishizawa, N., 1995. Electron density and optical anisotropy in rhombohedral carbonates. III. Synchrotron Xray studies of CaCO3, MgCO3 and MnCO3. Acta Crystallogr. Sect. B 51, 929–939. https://doi.org/10.1107/S0108768195006434.

Matekonis, G., Šiaučiūnas, R., Vaičiukynienė, D., 2010. Hydrothermal Synthesis and Characterization of Na + and [Al 3 + + Na +] -substituted Tobermorite in CaO-SiO2·nH2O-H2O System. Mater. Sci. 16, 242–248.

Matsui, K., Kikuma, J., Tsunashima, M., Ishikawa, T., Matsuno, S., Ogawa, A., Sato, M., 2011. In situ time-resolved X-ray diffraction of tobermorite synthesis process under hydrothermal condition. IOP Conf. Ser. Mater. Sci. Eng. 18, 60–66. https://doi.org/10.1088/1757-899X/18/2/022017.

Merlino, S., Bonaccorsi, E., Armbruster, T., 2000. The real structures of clinotobermorite and tobermorite 9 Å: OD character, polytypes, and structural relationships. Eur. J. Mineral. 12, 411–429. https://doi.org/10.1127/0935-1221/2000/0012-0411.

Monasterio, M., Gaitero, J.J., Manzano, H., Dolado, J.S., Cerveny, S., 2015. Effect of chemical environment on the dynamics of water confined in calcium silicate minerals: Natural and synthetic tobermorite. Langmuir 31, 4964–4972. https://doi.org/10.1021/acs.langmuir.5b00614.

Mostafa, N.Y., 2005. Influence of air-cooled slag on physicochemical properties of autoclaved aerated concrete. Cem. Concr. Res. 35, 1349–1357. https://doi.org/10.1016/j.cemconres.2004.10.011.

Mostafa, N.Y., Shaltout, A.A., Omar, H., Abo-El-Enein, S.A., 2009. Hydrothermal synthesis and characterization of aluminium and sulfate substituted 1.1 nm tobermorites. J. Alloys Compd. 467, 332–337. https://doi.org/10.1016/j.jallcom.2007.11.130.

Naber, C., Stegmeyer, S., Jansen, D., Goetz-Neunhoeffer, F., Neubauer, J., 2019. The PONKCS method applied for time resolved XRD quantification of supplementary cementitious material reactivity in hydrating mixtures with ordinary Portland cement. Constr. Build. Mater. 214, 449–457. https://doi.org/10.1016/j.conbuildmat.2019.04.157.

Qu, X., Zhao, Z., Zhao, X., 2018. Microstructure and characterization of aluminum-incorporated calcium silicate hydrates (C-S-H) under hydrothermal conditions. RSC Adv. 8, 28198–28208. https://doi.org/10.1039/c8ra04423f.

Rashad, A.M., 2013. Metakaolin as cementitious material: history, scours, production and composition - a comprehensive overview. Constr. Build. Mater. 41, 303–318. https://doi.org/10.1016/j.conbuildmat.2012.12.001.

Rietveld, H.M., 1969. A profile refinement method for nuclear and magnetic structures. J. Appl. Crystallogr. 2, 65–71. https://doi.org/10.1107/S0021889869006558.

Ríos, C.A., Williams, C.D., Fullen, M.A., 2009. Hydrothermal synthesis of hydrogarnet and tobermorite at 175 °C from kaolinite and metakaolinite in the CaO-Al2O3-SiO2-H2O system: a comparative study. Appl. Clay Sci. 43, 228–237. https://doi.org/10.1016/j.clay.2008.09.014.

Różycka, A., Pichór, W., 2016. Effect of perlite waste addition on the properties of autoclaved aerated concrete. Constr. Build. Mater. 120, 65–71. https://doi.org/10.1016/j.conbuildmat.2016.05.019.

Rózycka, A., Kotwica, Ł., Małolepszy, J., 2014. Synthesis of single phase gyrolite in the CaO-quartz-Na2O-H2O system. Mater. Lett. 120, 166–169. https://doi.org/10.1016/j.matlet.2014.01.003.

Sauman, Z., 1974. Influence of SO4 2– ions on the formation of 11 Å tobermorite. In: Proceedings of the 2nd International Symposium on Science and Research in Silicate Chemistry. Moscow, pp. 25–39.

Schmidt, M., Egersdörfer, A., Pöllmann, H., 2012. Increased reactivity: using a glass-containing metakaolin as an active filler in lime-based binder systems. ZKG Int. 65, 54–62.

Schreiner, J., Jansen, D., Ectors, D., Goetz-Neunhoeffer, F., Neubauer, J., Volkmann, S., 2018. New analytical possibilities for monitoring the phase development during the production of autoclaved aerated concrete. Cem. Concr. Res. 107, 247–252. https://doi.org/10.1016/j.cemconres.2018.02.028.

Schreiner, J., Goetz-Neunhoeffer, F., Neubauer, J., Volkmann, S., Bergold, S., Webler, R., Jansen, D., 2019. Advanced Rietveld refinement and SEM analysis of tobermorite in chemically diverse autoclaved aerated concrete. Powder Diffract. 34, 143–150. https://doi.org/10.1017/s0885715619000149.

Setthaya, N., Chindaprasirt, P., Pimraksa, K., 2016. Preparation of zeolite nanocrystals via hydrothermal and solvothermal synthesis using of rice husk ash and metakaolin. Mater. Sci. Forum 872, 242–247. https://doi.org/10.4028/www.scientific.net/msf.872.242.

Siauciunas, R., Baltakys, K., 2004. Formation of gyrolite during hydrothermal synthesis in the mixtures of CaO and amorphous SiO2 or quartz. Cem. Concr. Res. 34, 2029–2036. https://doi.org/10.1016/j.cemconres.2004.03.009.

Skawinska, A., Owsiak, Z., Baran, T., Hernik, K., 2017. The influence of halloysite addition on tobermorite formation in CaO and quartz mix under hydrothermal conditions. Cem. Wapno Bet. 17, 426–434.

Venhodová, E., Janovský, R., Drochytka, R., 2015. Formation of tobermorite at different materials composition of aerated concrete. Appl. Mech. Mater. 752–753, 247–250. https://doi.org/10.4028/www.scientific.net/amm.752-753.247.

Walczak, P., Małolepszy, J., Reben, M., Szymański, P., Rzepa, K., 2015. Utilization of waste glass in autoclaved aerated concrete. Proc. Eng. 122, 302–309. https://doi.org/10.1016/j.proeng.2015.10.040.

Zhang, Y., Gao, W., Cui, L., 2007. The transformation of acid leached metakaolin to zeolite beta. Stud. Surf. Sci. Catal. 170, 420–425. https://doi.org/10.1016/S0167-2991(07)80870-6.

Zvyagin, B.B., 1960. An attempt to electronographic determination of kaolinite structure. J. Dokl. Akad. Nauk SSSR 130, 1023–1026.

6.2 Advanced Rietveld refinement and SEM analysis of tobermorite in chemically diverse autoclaved aerated concrete

Following the copyright guidelines by Cambridge University Press, the publication

Schreiner, J., Goetz-Neunhoeffer, F., Neubauer, J., Volkmann, S., Bergold, S., Webler, R., Jansen, D., 2019. Advanced Rietveld refinement and SEM analysis of tobermorite in chemically diverse autoclaved aerated concrete. Powder Diffraction **34**, 143–150. https://doi.org/10.1017/s0885715619000149

may not be reprinted. It can be accessed at:

https://www.cambridge.org/core/journals/powder-diffraction/article/advanced-rietveld-refinement-and-sem-analysis-of-tobermorite-in-chemically-diverse-autoclaved-aerated-concrete/51597C2A66F6F225D29DEB2675E74249

6.3 New analytical possibilities for monitoring the phase development during the production of autoclaved aerated concrete

Reprint of the peer reviewed publication

Schreiner, J., Jansen, D., Ectors, D., Goetz-Neunhoeffer, F., Neubauer, J., Volkmann, S., 2018. New analytical possibilities for monitoring the phase development during the production of autoclaved aerated concrete. Cement and Concrete Research **107**, 247–252. https://doi.org/10.1016/j.cemconres.2018.02.028

with permission from Elsevier.

Cement and Concrete Research 107 (2018) 247–252

Contents lists available at ScienceDirect

Cement and Concrete Research

journal homepage: www.elsevier.com/locate/cemconres

Short communication

New analytical possibilities for monitoring the phase development during the production of autoclaved aerated concrete

J. Schreiner[a,*], D. Jansen[a,*], D. Ectors[a], F. Goetz-Neunhoeffer[a], J. Neubauer[a], S. Volkmann[b]

[a] University of Erlangen-Nuremberg, GeoZentrum Nordbayern, Mineralogy, Schlossgarten 5a, 91054 Erlangen, Germany
[b] Rodgauer Baustoffwerke GmbH & Co. KG, Am Opel-Prüffeld 3, 63110 Rodgau-Dudenhofen, Germany

A B S T R A C T

This work presents improved analytical methods for both steps of the production process of autoclaved aerated concrete (AAC), the phase development during the hydration before autoclaving and during the autoclaving process itself. The improvement includes new insights into preparation methods of AAC samples for powder diffraction as well as Rietveld refinement strategies. For the first time a new implementation for calculating anisotropic crystal domain sizes is applied to major hydrate phases occurring during AAC production, namely portlandite during the hydration before autoclaving and tobermorite during the autoclaving process. The calculation of anisotropic domain size growth, which can be implemented in the Rietveld environment, is based on crystallographically and geometrically appropriate models. The implementation of calculating anisotropic domain sizes for the Rietveld software TOPAS 5.0 allows a superior Rietveld fit and a more accurate quantification of the phase development. Additionally it enables the tracking of growth mechanism of portlandite during hydration.

1. Introduction

Autoclaved aerated concrete (AAC) is known as a lightweight construction material, which offers outstanding properties such as sufficient strength for construction in addition with excellent thermal insulation [1,2]. AAC is produced by autoclaving from calcareous raw materials such as lime (CaO) and cement, quartz, sulfate carrier and other additives such as foaming agents and water.

The production process (Fig. 1) can be separated into the hydration of the mixed slurry before the procedure of autoclaving and the autoclaving at elevated temperature (180 °C to 200 °C) under saturated steam pressure (1.2 MPa) for several hours.

The hydration process before autoclaving is necessary to achieve sufficient strength in order to cut the green cake blocks, as they should have a specific shape and dimension after autoclaving. Furthermore, the porous structure is generated by the foaming agent during hydration in the first process step. During autoclaving the final properties namely strength and low thermal conductivity are achieved.

It is already well understood that the autoclaving process leads to the formation of several phases, first of all tobermorite ($Ca_5Si_6O_{16}(OH)_2$*$4H_2O$) [3–5]. Newest research has shown impressively which reactions are running from the mineralogical point of view. Insitu XRD measurements were carried out during the autoclaving process and the phase development was shown by plotting normalized intensities [6]. The study of Mitsuda et al. [3] was mainly focused on the tracking of the phase evolution during the autoclaving process of AAC. However, their statements concerning phase evolution are mainly based on XRD data and TGA measurements. There is a common agreement that the following reactions occur. The consumption of the alite (OPC) leads to the formation of an initial C-S-H phase during the first processing step. Portlandite, which was initially formed during the first process step (from CaO and C_3S), further quartz and the C-S-H phase are consumed during autoclaving resulting in the crystallization of tobermorite. Hence, the crystallization process of tobermorite as well as the crystal structure of tobermorite was an issue of research and discussion over the last years and numerous publications to these topics are available. Concerning the crystal structure of tobermorite, respectively the tobermorite supergroup, a new publication outlines all important references and recommends a new nomenclature [7].

The presented study was performed to create new analytical possibilities for the characterization of the production process of AAC. Both of the production process steps are essential for the final product. Hence, the present work focuses on crystallization of hydrate phases in both processes.

Firstly, an external standard method [8,9] was published and

* Corresponding authors.
E-mail addresses: juergen.js.schreiner@fau.de (J. Schreiner), daniel.jansen@fau.de (D. Jansen).

https://doi.org/10.1016/j.cemconres.2018.02.028
Received 6 October 2017; Received in revised form 1 February 2018; Accepted 26 February 2018

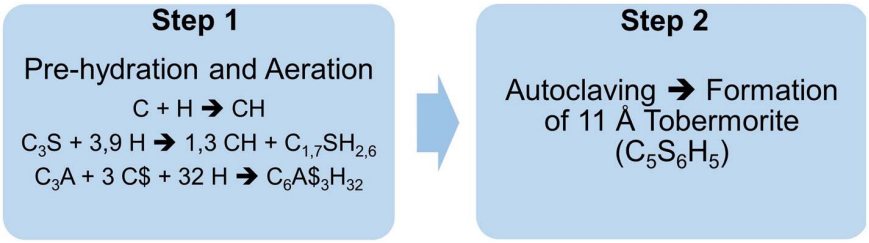

Fig. 1. Simplified process steps of AAC production and hydrate phase evolution.

recommended for the determination of absolute phase contents in mixtures with amorphous content. It was shown that the method can absolutely be recommended for hydrating cement pastes in which water cannot be quantified directly by XRD [10]. This method seems to be very promising for both, the quantification of the hydration of the AAC slurry before autoclaving and the quantification of the phase evolution during autoclaving inasmuch as both production steps form crystalline and amorphous phases.

Secondly, a new approach to anisotropic peak broadening due to anisotropic domain morphology, which was developed [11,12], is applied to AAC samples to improve the fit of portlandite and tobermorite by Rietveld refinement [13]. By applying this approach, the refinement of both portlandite and tobermorite should additionally lead to better quantitative results as well as to better insights into the development of the domain size morphology of both phases formed.

It was already shown that in a hydrating raw mixture for AAC, two species of portlandite precipitate at 23 °C, one showing dynamically anisotropic peak broadening and another one following the isotropic trend [14]. The application of the anisotropic refinement model led to an improved fitting of portlandite. Moreover the mechanism of anisotropic domain growth of portlandite was tracked.

2. Materials and methods

In order to examine the hydration of the AAC slurry before autoclaving a mixture of the hydraulic reactive components was weighed and measured in-situ at a Bruker D8 diffractometer with a LynxEye detection system.

Ordinary Portland cement (OPC) was mixed with lime (CaO) and anhydrite (C$). The raw materials were taken from the same batches as for the industrial samples. The drymix (58% OPC, 36% CaO and 6% C$ by weight) was then mixed with water (w/s = 0.8) and placed into an appropriate sample holder. The samples were not aerated. The slurry samples were covered with a kapton film to avoid evaporation and carbonation. Diffractograms were recorded with an angular range from 7 to 54,5° 2θ and a step width of 0,011° 2θ. Measurements were carried out every 15 min. For each measurement 96 XRD patterns were recorded over the first 24 h. The temperature was fixed at 70 °C, which is the mean temperature generally prevailing in the industrial process during hydration before autoclaving. Rietveld refinement was carried out using the G-factor method. All structures used for Rietveld refinement are shown in Table 1.

For investigation of the autoclaved samples, five different specimens were taken at different autoclaving times. The specimens were taken out of a technical production process, hence it was not possible to interrupt the process at an earlier time inasmuch it would lead to damage of a whole concrete production batch. The specimens were firstly dried at 60 °C until weight constancy. The whole blocks were then broken and statistical samples of 20 g were taken. In order to receive the right mass attenuation coefficient (MAC) for G-factor method, the loss on ignition and the chemical composition (XRF) were determined. For energy dispersive XRF analysis (Spectro Xepos) tube voltage from 20 kV to 50 kV and tube current from 0,8 to 2,0 mA were used for different targets.

Table 1
Structures used for Rietveld refinement.

Phase	Author
Alite	[15]
Anhydrite	[16]
Bassanite	[17]
Belite (β)	[18]
Belite (α′)	[19]
Brownmillerite	[20]
C-S-H	[21]
Calcite	[22]
Ettringite	[23]
Gypsum	[24]
Hemicarbonate	[25]
Hydroxylellestadite	[26]
Lime (CaO)	[27]
Microcline	[28]
Portlandite	[29]
Quartz	[30]
Tobermorite	[31]
Tricalciumaluminate (cubic)	[32]
Tricalciumaluminate (orthorhombic)	[33]
PONCKS model for Water	[21]

The final sample preparation (grinding) before XRD measurements was carried out using both, an agate mortar and a McCrone micronizing mill for wet milling with isopropanol. Both preparation methods were applied separately to see which one is suitable in order to get the best preparation for XRD investigations. Six preparations were performed by one operator, of which two were prepared with an agate mortar and four with a McCrone mill. For the McCrone milling 3 g of the sample and 10 ml of isopropanol were used for grinding for 12 min. The grain size distribution of one sample prepared with an agate mortar and one sample prepared using a McCrone mill was measured by laser granulometry in isopropanol using a Mastersizer 3000 (MALVERN).

After milling the samples in these two ways for XRD analysis the powders were prepared into a front loading sample holder and measured. Diffractograms were recorded with an angular range from 6 to 80° 2θ, a step width of 0,0236° 2θ and a time per step of 0,54 s. Rietveld refinement combined with external standard (G-factor) was applied in order to get absolute quantities for each phase. The refinement strategy for portlandite and tobermorite in the TOPAS Launch Mode (TOPAS 5.0, Bruker AXS) is attached as a Supplementary material file.

3. Results and discussion

3.1. Hydration of the mixture before autoclaving

The hydration of the investigated paste before autoclaving is dominated by the hydration of the cement as well as the reaction of the free lime (CaO) resulting in the formation of portlandite. It can be clearly seen from Fig. 2 that the hydration of the paste leads to the formation of ettringite, portlandite and C-S-H phase. For simplification, the remaining phase developments are not shown in Fig. 2 because they are not in the focus of this study. The hydration of CaO forming

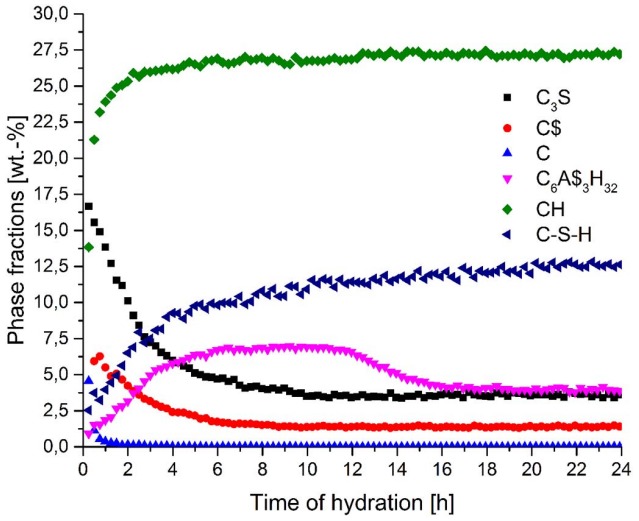

Fig. 2. Phase development in AAC paste on a laboratory scale before autoclaving analyzed by in-situ XRD at 70 °C.

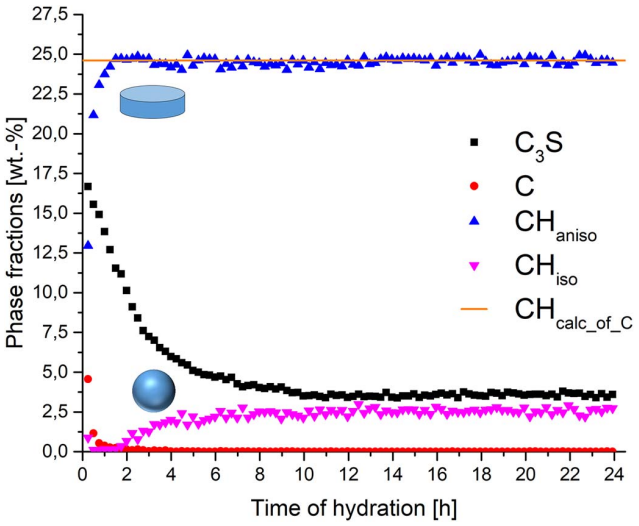

Fig. 3. Formation of two generations of portlandite by hydration of lime (1st) and C_3S (2nd) at 70 °C before autoclaving with the major generation showing anisotropic peak broadening.

portlandite begins rapidly after the addition of water to the mixture and lime is fully consumed after only 1 h of hydration. This translates into a quick rise of heat of hydration so that cement hydration is accelerated, which leads to further portlandite formation by the reaction of alite. Ettringite formation stalls after few hours of hydration. After 12 h ettringite is partially decomposed, probably due to sulfate depletion [9]

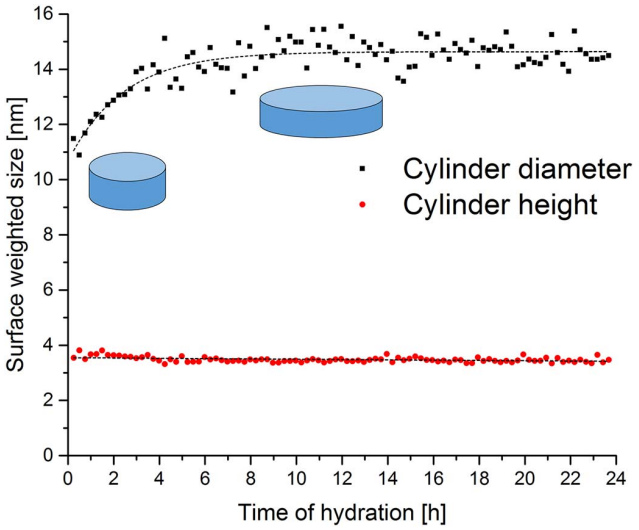

Fig. 5. Morphological evolution of portlandite showing anisotropic domain size growth during hydration at 70 °C.

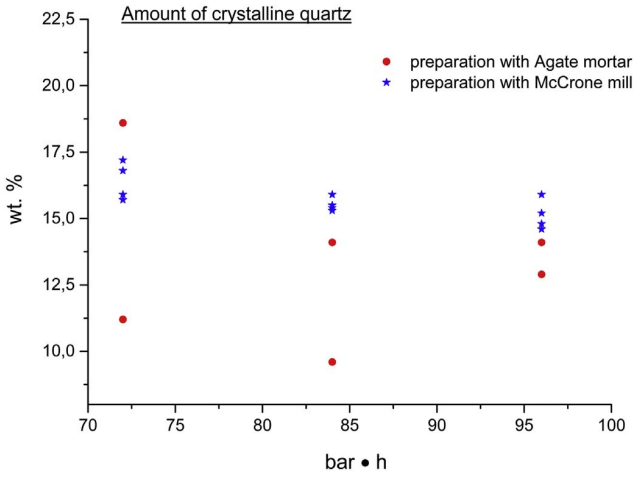

Fig. 6. Comparison of quantification of crystalline quartz in samples prepared with McCrone mill and agate mortar at different autoclaving times.

and poorly crystalline AFm phases (not shown in Fig. 2) are formed.

In Fig. 3, it can be seen that in fact two generations of portlandite are formed, a 1st dominant generation showing anisotropic peak broadening and 2nd one occurring considerably later following the isotropic domain size refinement, which is usually carried out using the Rietveld method. This occurrence comes along firstly with lime hydration and secondly with alite hydration. The expected quantity of portlandite formed from lime hydration very well complies with the

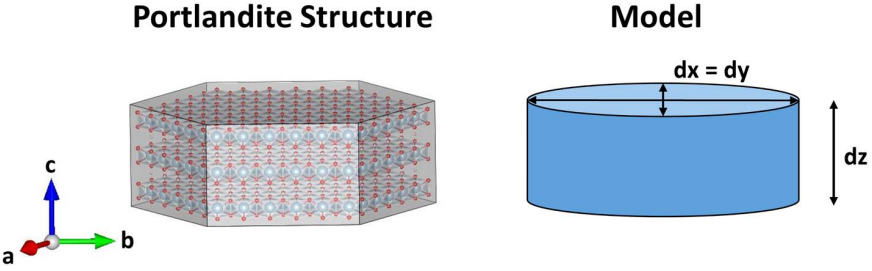

Fig. 4. Biaxial cylinder domain size model of portlandite used for Rietveld refinement of anisotropic peak broadening.

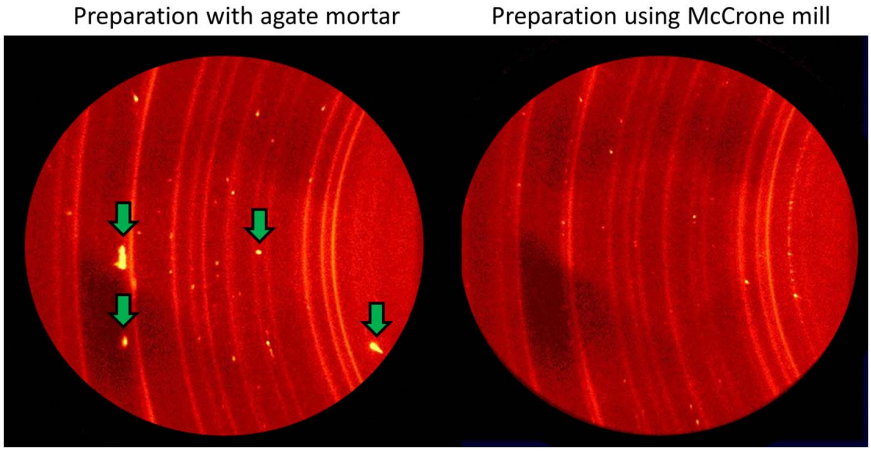

Fig. 7. 2D XRD with Bruker GADDS-system plots of samples prepared with agate mortar and McCrone mill. Coarse quartz grains are pointed out in the plot of the sample prepared with agate mortar.

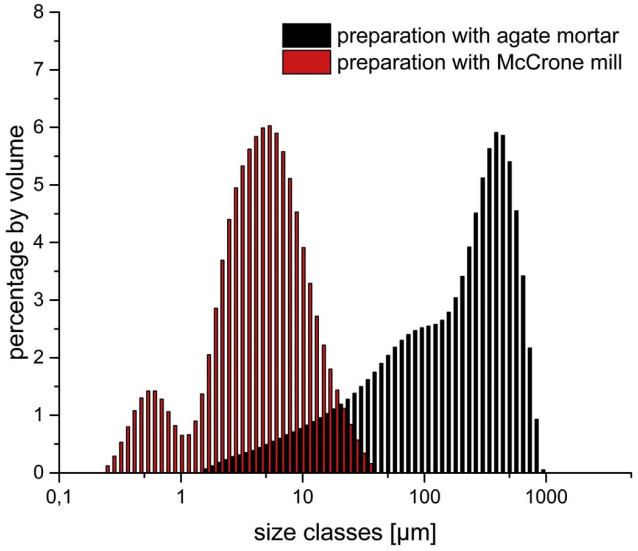

Fig. 8. Particle size distribution of one sample prepared with an agate mortar and of one sample prepared with a McCrone mill measured by laser granulometry.

quantity of the observed 1st generation. The development of portlandite growth was already tracked in an equivalent slurry at 23 °C [14]. Thus, this observation confirms that the crystallinity of portlandite in mixtures for AAC production depends on the starting phase for hydration, as already indicated by Ectors [14].

Fig. 4 shows the used biaxial cylindrical model for anisotropic domain size calculation and the portlandite structure, which was created with structural software VESTA 3.1.8 [34]. Using the cylindrical approach, domain sizes in a (here equating to b) and c direction (dz = cylinder height) can be calculated, which comes along with the expected symmetrical parameters of portlandite.

The 1st portlandite generation showing anisotropic domain growth can be tracked in terms of cylinder diameter and height, which is realized in Fig. 5. The blue cylinder represents the geometric approach and cylinder height and diameter are calculated newly for each range. The cylinder height remains rather stable throughout the hydration process, while the cylinder diameter increases during the first hours of hydration. After 10 h of hydration the mean cylinder diameter no longer increases. Consequently, these observations match the results of the examinations conducted at 23 °C [14], as well as the assumption, that different mechanisms of growth exist for portlandite depending on the

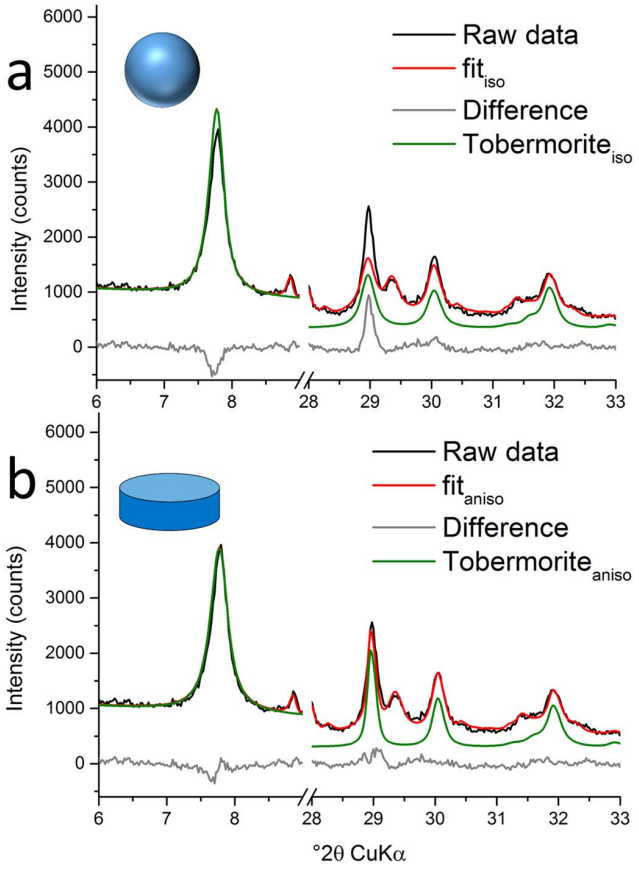

Fig. 9. Rietveld refinement for Tobermorite of autoclaved AAC sample by use of isotropic domain size model (a) and of anisotropic domain size model (b).

hydration educt. The maximum cylinder diameter is reached earlier in this work very likely because of the higher hydration temperature.

3.2. Quantification of the reactions during autoclaving

Autoclaved samples were ground with an agate mortar and compared to samples, which were wet-ground with a McCrone mill. Fig. 6 shows precisely that the determination of the amount of crystalline quartz is more reproducible in the two shown samples, which were

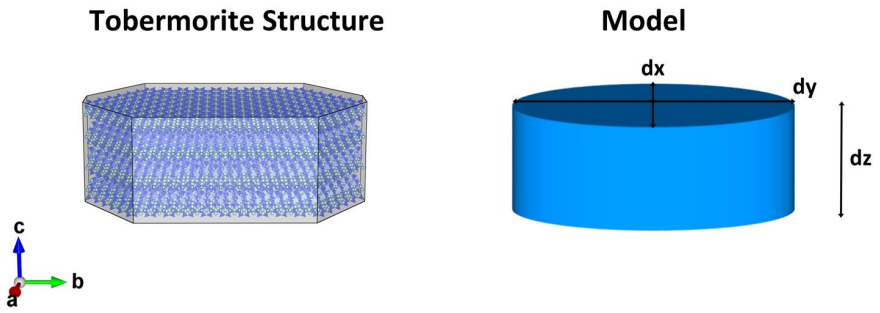

Fig. 10. Triaxial cylinder domain size model of Tobermorite used for Rietveld refinement of anisotropic peak broadening.

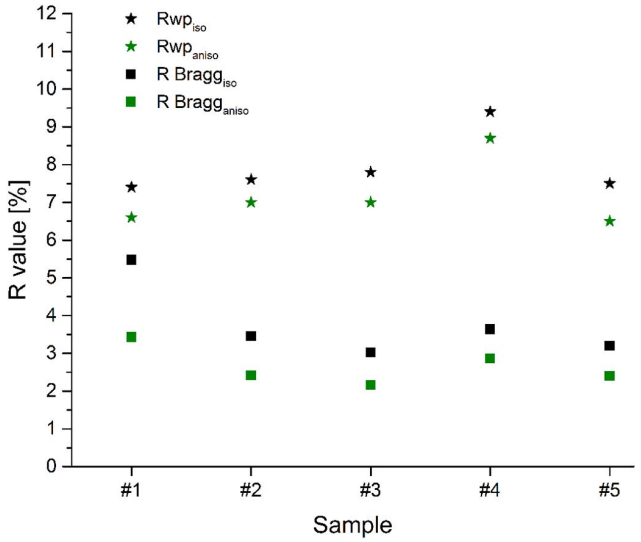

Fig. 11. Comparison of R_{wp} and R_{Bragg} values of Rietveld refinements of autoclaved samples and tobermorite using the isotropic and the anisotropic domain size model.

prepared with a McCrone mill. The high variance of crystalline quartz in the samples, which were prepared with an agate mortar, is a result of insufficient grinding and remaining of too large quartz grains. When this spottiness occurs, a reliable quantification using the G-factor method is not possible.

The 2D XRD with Bruker GADDS-system plots in Fig. 7 demonstrate the insufficient grinding when using an agate mortar compared to wet milling with a McCrone mill. Quartz would be overrepresented in a one-dimensional XRD pattern focusing on a section with bright spots (green arrows). The lack of bright spots in the right plot shows that the quartz grains are milled more thoroughly using a McCrone mill. In Fig. 8 the particle size distribution after both ways of sample preparation is compared. Most grains in the sample prepared with an agate mortar are larger than in the sample prepared with a McCrone mill. The grain size distribution of the sample prepared with a McCrone mill complies with the recommended particle size range for XRD analysis of under 5 to 50 µm [35,36], while the other sample exceeds the range.

In Fig. 9 Rietveld refinement of an autoclaved sample is shown. The dominant peaks at 7.7, 29.0 and 30.1° 2θ are attributed to tobermorite. In the upper diagram (a), Rietveld refinement was carried out regularly calculating isotropic domain sizes for tobermorite. However, the calculated fit differs significantly from the raw data. It can be assumed that tobermorite shows a similar pattern to portlandite in terms of anisotropic peak broadening, taking into account that tobermorite is assigned to the orthorhombic crystal system. Thus, instead of a biaxial cylinder model, an elliptic cylinder model (Fig. 10, structure created with VESTA 3.1.8 [34]) was applied for the refinement in the lower diagram (b). The elliptic cylinder model is a sufficient approach to the orthorhombic crystal system as it allows the distinction between domain sizes in a, b and c direction. The fit is clearly superior using the anisotropic domain size model, highlighted by the difference plot in Fig. 9b. The comparison refinement with isotropic and anisotropic approach was done for all of the five autoclaved samples. In Fig. 11, the resulting R_{wp} values for the whole pattern and the R_{Bragg} values of tobermorite are shown. The refinement using the anisotropic model leads to both, lower R_{wp} and R_{Bragg} values and consequently to a better fit and a more accurate quantification of tobermorite in all refined samples.

4. Summary and conclusions

Improved analytical methods for both, the phase development during the hydration before autoclaving and during the autoclaving process of AAC are presented. It could be shown that wet McCrone milling is the best way of preparation of AAC samples in order to obtain suitable samples for powder diffraction. A new approach to treat anisotropic domain sizes for Rietveld refinement could be successfully applied – with the benefit that portlandite and tobermorite in AAC samples could be refined more accurately using the Rietveld method. Thus, this application allows an improved quantification of the phase development during both of the production steps.

For the future, there are still plenty of possibilities to apply the presented approach of calculating anisotropic domain sizes to AAC production. As exemplified with portlandite, the mechanisms of growth of tobermorite can be tracked likewise during the autoclaving process. In addition, the effect of variations in the chemical composition of AAC raw mixtures on the crystal morphology of tobermorite can be examined. This leaves a new perspective to discuss the link between mineral phase morphology and the thermal and mechanical properties of AAC.

Acknowledgement

The autoclaved samples were generously provided by Rodgauer Baustoffwerke GmbH & Co. KG. The authors express gratitude for all support.

Appendix A. Supplementary data

Supplementary data to this article can be found online at https://doi.org/10.1016/j.cemconres.2018.02.028.

References

[1] M.W. Grutzeck, Cellular concrete, in: M. Scheffler, P. Colombo (Eds.), Cellular Ceramics, Wiley-VCH, Weinheim, 2005, pp. 193–223.
[2] M. Haas, The future of AAC – from a material scientist's point of view, in: M.C. Limbachiya, J.J. Roberts (Eds.), Autoclaved Aerated Concrete, Taylor Fr. London, 2005, pp. 187–194.
[3] T. Mitsuda, K. Sasaki, H. Ishida, Phase evolution during autoclaving process of aerated concrete, J. Am. Ceram. Soc. 75 (1992) 1858–1863.
[4] N. Isu, H. Ishida, T. Mitsuda, Influence of quartz particle size on the chemical and

mechanical properties of autoclaved aerated concrete (I) tobermorite formation, Cem. Concr. Res. 25 (1995) 243–248.
[5] N.Y. Mostafa, Influence of air-cooled slag on physicochemical properties of autoclaved aerated concrete, Cem. Concr. Res. 35 (2005) 1349–1357, http://dx.doi.org/10.1016/j.cemconres.2004.10.011.
[6] K. Matsui, J. Kikuma, M. Tsunashima, T. Ishikawa, S. Matsuno, A. Ogawa, M. Sato, In situ time-resolved X-ray diffraction of tobermorite formation in autoclaved aerated concrete: influence of silica source reactivity and Al addition, Cem. Concr. Res. 41 (2011) 510–519.
[7] C. Biagioni, S. Merlino, E. Bonaccorsi, The tobermorite supergroup: a new nomenclature, Mineral. Mag. 79 (2015) 485–495, http://dx.doi.org/10.1180/minmag.2015.079.2.22.
[8] B.H. O'Connor, M.D. Raven, Application of the Rietveld refinement procedure in assaying powdered mixtures, Powder Diffract. 3 (1988) 2–6, http://dx.doi.org/10.1017/S0885715600013026.
[9] D. Jansen, F. Goetz-Neunhoeffer, C. Stabler, J. Neubauer, A remastered external standard method applied to the quantification of early OPC hydration, Cem. Concr. Res. 41 (2011) 602–608, http://dx.doi.org/10.1016/j.cemconres.2011.03.004.
[10] D. Jansen, C. Stabler, F. Goetz-Neunhoeffer, S. Dittrich, J. Neubauer, Does Ordinary Portland Cement contain amorphous phase? A quantitative study using an external standard method, Powder Diffract. 26 (2011) 31–38, http://dx.doi.org/10.1154/1.3549186.
[11] D. Ectors, F. Goetz-Neunhoeffer, J. Neubauer, A generalized geometric approach to anisotropic peak broadening due to domain morphology, J. Appl. Crystallogr. 48 (2015) 189–194, http://dx.doi.org/10.1107/S1600576714026557.
[12] D. Ectors, F. Goetz-Neunhoeffer, J. Neubauer, Routine (an)isotropic crystallite size analysis in the double-Voigt approximation done right? Powder Diffract. 32 (S1) (2017) 27–34, http://dx.doi.org/10.1017/S0885715617000070.
[13] H.M. Rietveld, A profile refinement method for nuclear and magnetic structures, J. Appl. Crystallogr. 2 (1969) 65–71, http://dx.doi.org/10.1107/S0021889869006558.
[14] D. Ectors, Advances in the Analysis of Cementitious Reactions and Hydrate Phases (Doctoral Thesis), (2016), pp. 12–14 (urn:nbn:de:bvb:29-opus4-71743).
[15] Á.G. De La Torre, S. Bruque, J. Campo, M.A.G. Aranda, The superstructure of C3S from synchrotron and neutron powder diffraction and its role in quantitative phase analyses, Cem. Concr. Res. 32 (2002) 1347–1356, http://dx.doi.org/10.1016/S0008-8846(02)00796-2.
[16] A. Kirfel, G. Will, Charge density in anhydrite, $CaSO_4$, from X-ray and neutron diffraction measurements, Acta Crystallogr. Sect. B: Struct. Crystallogr. Cryst. Chem. 36 (1980) 2881–2890, http://dx.doi.org/10.1107/S0567740880010461.
[17] C. Bezou, A.N. Christensen, D. Cox, M. Lehman, A. Nonat, Structures cristallines de $CaSO_4.0.5H_2O$ et $CaSO_4.0.6H_2O$, Comptes Rendus Hebd, Des Séances l'Académie Des Sci. Série 2 (312) (1991) 43–48.
[18] K.H. Jost, B. Ziemer, R. Seydel, Redetermination of the structure of β-dicalcium silicate, Acta Crystallogr. Sect. B: Struct. Crystallogr. Cryst. Chem. 33 (1977) 1696–1700, http://dx.doi.org/10.1107/S0567740877006918.
[19] W. Mumme, L.M.D. Cranswick, B.C. Chakoumakos, Rietveld crystal structure refinements from high temperature neutron powder diffraction data for the polymorphs of dicalcium silicate, Neues Jahrb. Fuer Mineral. Abhandlungen 170 (1996) 171–188.
[20] A. Colville, S. Geller, The crystal structure of brownmillerite, Ca_2FeAlO_5, Crystallographica 50 (1971) 2311–2315, http://dx.doi.org/10.1107/S056774087100579X.
[21] S.T. Bergold, F. Goetz-Neunhoeffer, J. Neubauer, Quantitative analysis of C-S-H in hydrating alite pastes by in-situ XRD, Cem. Concr. Res. 53 (2013) 119–126, http://dx.doi.org/10.1016/j.cemconres.2013.06.001.
[22] E.N. Maslen, V.A. Streltsov, N.R. Streltsova, N. Ishizawa, Electron density and optical anisotropy in rhombohedral carbonates. III. Synchrotron Xray studies of $CaCO_3$, $MgCO_3$ and $MnCO_3$, Acta Crystallogr. Sect. B 51 (1995) 929–939, http://dx.doi.org/10.1107/S0108768195006434.
[23] G. Renaudin, Y. Filinchuk, J. Neubauer, F. Goetz-Neunhoeffer, A comparative structural study of wet and dried ettringite, Cem. Concr. Res. 40 (2010) 370–375, http://dx.doi.org/10.1016/j.cemconres.2009.11.002.
[24] W.F. Cole, C.J. Lancucki, A refinement of the crystal structure of gypsum $CaSO_4.2H_2O$, Acta Cryst B30 (1974) 921–929, http://dx.doi.org/10.1107/S0567740874004055.
[25] T. Runčevski, R.E. Dinnebier, O.V. Magdysyuk, H. Pöllmann, Crystal structures of calcium hemicarboaluminate and carbonated calcium hemicarboaluminate from synchrotron powder diffraction data, Acta Crystallogr. Sect. B: Struct. Sci. 68 (2012) 493–500, http://dx.doi.org/10.1107/S010876811203042X.
[26] J.M. Hughes, J.W. Drexler, Cation substitution in the apatite tetrahedral site: crystal structures of type hydroxylellestadite and type fermorite, Neues Jahrb. Fuer Mineral (1991) 327–336.
[27] C.H. Shen, R.S. Liu, J.G. Lin, C.Y. Huang, Phase stability study of $La_{1.2}Ca_{1.8}Mn_2O_7$, Mater. Res. Bull. 36 (2001) 1139–1148.
[28] S.W. Bailey, Refinement of an intermediate microcline structure, Am. Miner. 54 (1969) 1540–1545.
[29] W.R. Busing, H.A. Levy, Neutron diffraction study of calcium hydroxide, J. Chem. Phys. 26 (1957) 563, http://dx.doi.org/10.1063/1.1743345.
[30] Y. Le Page, G. Donnay, Refinement of the crystal structure of low-quartz, Acta Crystallogr. Sect. B 32 (1976) 2456–2459, http://dx.doi.org/10.1107/S0567740876007966.
[31] S.A. Hamid, The crystal structure of the 11 Å natural tobermorite $Ca_{2.25}[Si_3O_{7.5}(OH)_{1.5}]1H_2O$, Zeitschrift Fuer Krist. - New Cryst. Struct. 154 (1981) 189–198, http://dx.doi.org/10.1524/zkri.1981.154.3-4.189.
[32] P. Mondal, J.W. Jeffery, The crystal structure of tricalcium aluminate, $Ca_3Al_2O_6$, Acta Crystallogr. B 31 (1975) 689–697, http://dx.doi.org/10.1107/S0567740875003639.
[33] Y. Takeuchi, F. Nishi, I. Maki, Crystal-chemical characterization of the tricalcium aluminate-sodium oxide ($3CaO \times Al_2O_3$-Na_2O) solid-solution series, Zeitschrift Für Krist (1980) 259–307.
[34] K. Momma, F. Izumi, VESTA 3 for three-dimensional visualization of crystal, volumetric and morphology data, J. Appl. Crystallogr. 44 (2011) 1272–1276, http://dx.doi.org/10.1107/S0021889811038970.
[35] K. Scrivener, R. Snellings, B. Lothenbach, A Practical Guide to Microstructural Analysis of Cementitious Materials, CRC Press, 2016, pp. 123–125, http://dx.doi.org/10.7693/wl20150205.
[36] V. Pecharsky, P. Zavalij, Fundamentals of Powder Diffraction and Structural Characterization of Materials, Springer, second edition, 2005, p. 302, http://dx.doi.org/10.1007/978-0-387-09579-0.

7 Acknowledgement

Ich möchte mich bei einigen Personen bedanken, ohne die es wohl kaum zum erfolgreichen Abschluss dieser Arbeit gekommen wäre.
Mein Doktorvater Prof. Dr. Jürgen Neubauer hat sich stets die Zeit genommen, die nötig war, um Angelegenheiten aller Art mit mir zu klären. Er gab mir fachlich immer zum richtigen Zeitpunkt einen gewissen wissenschaftlichen Impuls. Zugleich habe ich mich dennoch immer frei in meiner eigenen Konzeption gefühlt. Großen Dank spreche ich Prof. Dr. Friedlinde Götz-Neunhoeffer aus, die für mich ebenso immer eine verlässliche Ansprechpartnerin für fachliche und organisatorische Angelegenheiten aller Art war. Danke an Dr. Daniel Jansen für die gute Zusammenarbeit und dafür, dass er mich im Zuge meiner Masterarbeit in ein Forschungsprojekt aufgenommen hat, das den Weg zur Promotion möglich machte. Zusätzlich gilt mein Dank Prof. Dr. Matthias Göbbels, der für die Mitarbeiter am Lehrstuhl immer motivierende Worte fand. Für die Ermöglichung meiner Teilnahme an diversen Dienstreisen, Fortbildungen und Tagungen möchte ich mich vielmals bedanken.
Weiterhin bedanke ich mich bei Dr. Stephan Volkmann und den Rodgauer Baustoffwerken GmbH & Co. KG für die gute Zusammenarbeit und die Bereitstellung von Versuchsmaterialien.
Vielen Dank an meine studentischen Hilfskräfte Daniel Wagner, Laura Moldenhauer, Fabian Lang, Jakob Schreiber und Felix Klaassen, die alle Aufgaben im Labor einwandfrei und mit Bedacht erledigten. Bei meinen aktuellen und ehemaligen Kollegen Dr. Katrin Hurle, Dr. Dominique Ectors, Dr. Christoph Naber, Dr. Florian Hüller, Jörg Nehring, Frank Riedel, Julian Wolf, Tanja Manninger, Daniel Wagner, Nicolas Fobbe, Karla Späth, Julian Goergens, Andreas Köhler, Cordula Jakob, Franz Becker und Lisa Klemenz bedanke ich mich für die gelungene Zusammenarbeit und gegenseitige Unterstützung. Besonderer Dank geht auch an Kerstin Kreß, Bettina Engl, Christian Hanke, Bernd Schleifer und Christian Abe für die verlässliche Unterstützung bei technischen Fragen und Messungen im Labor.
Für jegliche Unterstützungen möchte ich mich auch bei meinen Eltern bedanken, sowie bei meinem Bruder Ralf, der mir mit einem LaTex Crashkurs viel Frustration erspart hat. Danke Thomas, dass du immer für mich da bist und mit mir zusammen für genug Ausgleich gesorgt hast.